Shearing and rotation of β'' and β' precipitates in an Al-Mg-Si alloy under tensile deformation : in-situ and ex-situ studies

Acta Materialia

Shearing and rotation of β″ and β′ precipitates in an Al-Mg-Si alloy under tensile deformation: In-situ and ex-situ studies

--Manuscript Draft--

Manuscript Number:	A-21-2047R1
Article Type:	Full length article
Keywords:	Precipitate; Fragments; interface; Dislocation-precipitate interaction; TEM
Corresponding Author:	Kai Li, Ph.D State Key Laboratory of Powder Metallurgy, Central South University, Changsha 410083, China Changsha, CHINA
First Author:	Mingjun Yang
Order of Authors:	Mingjun Yang
	Andrey Orekhov
	Zhi-Yi Hu
	Man Feng
	Shenbao Jin
	Gang Sha
	Kai Li, Ph.D
	Vahid Samaee
	Min Song
	Yong Du
	Gustaaf Van Tendeloo
	Dominique Schryvers
Abstract:	The interaction between dislocations and nano-precipitates during deformation directly influences hardening response of precipitation-strengthening metals such as Al-Mg-Si alloys. However, how coherent and semi-coherent nano-precipitates accommodate external deformation applied to an Al alloy remains to be elucidated. In-situ tensile experiments in a transmission electron microscope (TEM) were conducted to study the dynamic process of dislocations cutting through coherent needle-like β″ precipitates with diameters of 3~8 nm. Comprehensive investigations using in-situ , ex-situ TEM and atom probe tomography uncovered that β″ precipitates were firstly sheared into small fragments, and then the rotation of the fragments, via sliding along precipitate/matrix interfaces, destroyed their initially coherent interface with the Al matrix. In contrast, semi-coherent β′ precipitates with sizes similar to β″ were more difficult to be fragmented and accumulation of dislocations at the interface increased interface misfit between β′ and the Al matrix. Consequently, β′ precipitates could basically maintain their needle-like shape after the tensile deformation. This research gains new insights into the interaction between nano-precipitates and dislocations.

Shearing and rotation of β″ and β′ precipitates in an Al-Mg-Si alloy under tensile deformation: *In-situ* and *ex-situ* studies

Mingjun Yang[1, †], Andrey Orekhov[2, †], Zhi-Yi Hu[3, 4], Man Feng[5], Shenbao Jin[5], Gang Sha[5], Kai Li[1, 6, *], Vahid Samaee[2], Min Song[1, 6], Yong Du[1, 6], Gustaaf Van Tendeloo[2, 4], Dominique Schryvers[2]

[1]State Key Laboratory of Powder Metallurgy, Central South University, Changsha 410083, China

[2]Electron Microscopy for Materials Science (EMAT), University of Antwerp, Antwerp B-2020, Belgium

[3]State Key Laboratory of Advanced Technology for Materials Synthesis and Processing, Wuhan University of Technology, Wuhan 430070, China

[4]NRC (Nanostructure Research Centre), Wuhan University of Technology, Wuhan 430070, China

[5]Herbert Gleiter Institute of Nanoscience, Nanjing University of Science and Technology, Nanjing 210094, China

[6]Advanced Research Center, Central South University, Changsha 410083, China

Abstract

The interaction between dislocations and nano-precipitates during deformation directly influences hardening response of precipitation-strengthening metals such as Al-Mg-Si alloys. However, how coherent and semi-coherent nano-precipitates accommodate external deformation applied to an Al alloy remains to be elucidated. *In-situ* tensile experiments in a transmission electron microscope (TEM) were conducted to study the dynamic process of dislocations cutting through coherent needle-like β″ precipitates with diameters of 3~8 nm. Comprehensive investigations using *in-situ*, *ex-situ* TEM and atom probe tomography uncovered that β″ precipitates

were firstly sheared into small fragments, and then the rotation of the fragments, via sliding along precipitate/matrix interfaces, destroyed their initially coherent interface with the Al matrix. In contrast, semi-coherent β′ precipitates with sizes similar to β″ were more difficult to be fragmented and accumulation of dislocations at the interface increased interface misfit between β′ and the Al matrix. Consequently, β′ precipitates could basically maintain their needle-like shape after the tensile deformation. This research gains new insights into the interaction between nano-precipitates and dislocations.

Key words: Precipitate; Fragments; Interface; Dislocation-precipitate interaction; TEM

†The two authors contribute to the work equally

*Corresponding authors. Tel: + 86 18973163497; email: leking@csu.edu.cn (K. Li);

1. Introduction

Precipitation of secondary phases plays a critical role in the mechanical properties of many alloys [1]. Densely distributed fine precipitates can cause precipitation strengthening by pinning gliding dislocations. Precipitation strengthening of Al-Mg-Si alloys has been intensively investigated since they are widely used in, e.g., the lightweight automobile industry. The precipitation sequence of Al-Mg-Si alloys is widely accepted as [2, 3]: super-saturated solid solution (SSSS) → atomic clusters → GP zones → β″ → β', U1, U2, B' → β, Si. Among these precipitates, β″ and β' are seen as coherent and semi-coherent precipitates, providing the largest and the second large contributions to alloy strength, respectively [4-7]. The mechanical properties of Al-Mg-Si based alloys are mainly determined by the impeding effect of precipitates on slide of dislocations, and precipitates are generally sheared or bypassed by gliding dislocations [7-15]. In addition to the inherent elastic properties (e.g., elastic modulus) and lattice misfit between the precipitate and matrix, the radius of a precipitate affects whether it can be sheared or bypassed by a gliding dislocation [16, 17].

Critical radius of precipitates r_c has been proposed for the transition from shearing to bypassing, but no precise value of r_c for β″ has been unanimously accepted by previous investigations. For instance, it was assumed to be 3.0 nm for a needle-like shape according to Esmaeili et al. [18], or 5.0 nm for an assumed spherical shape (for simplification) according to Myhr et al. [19]. Further *ex-situ* investigations on deformed Al-Mg-Si-Cu alloys have shown that needle-like β″ precipitates with a radius range from 1.8 nm to 2.5 nm can be sheared by dislocations [13, 20], while some other work

pointed out that β″ precipitates are shearable regardless of their size [13, 14]. This confliction remains to be solved. Compared to β″ precipitates, β′ precipitates were seen to be sheared when the longest dimension of their cross-section was shorter than approximately 15 nm, and looped otherwise [7].

Dislocation shearing can drastically change the morphologies and orientations of precipitates. For example, it has been reported that both needle-like $MgZn_2$ (diameter ~70 nm) and plate-like θ-Al_2Cu (thickness ~8 nm and width of several hundred nm) precipitates in aluminum alloys can be fragmented into very small spherical particles during equal-channel angular pressing (ECAP) [21, 22], and the observed polycrystalline diffraction rings of precipitates revealed their rotation alongside dislocation shearing. Besides, the gliding of dislocations inside the semi-coherent plate-like precipitates (thickness ~11 nm) in a two-phase Ni-Co superalloy was found to cause rotation of its central part, which was oppositely sheared between two positions where the distance was smaller than the precipitate thickness [23]. The corresponding shift was as large as half the thickness of the precipitate. It should be noted that residual dislocations were produced at the entrance and exit sites of the principal shear at the initial state of deformation, and their Burgers vectors are different from that of the matrix or the precipitate. Furthermore, the interaction between these residual dislocations with the secondary shear created stacking faults within the precipitate. The accumulation of stacking faults leads to the rotation of the central part of the precipitate. In their work [23], the rotated central part and the un-rotated remaining parts were still connected, i.e. the precipitate was not broken-apart.

As for fine needle-like precipitates, e.g. those with diameters smaller than 10 nm in Al-Mg-Si alloys, little is known about their behaviors after dislocations start to shear them. β″ precipitates under shearing of dislocations in 20% compressed Al-Mg-Si samples have been studied by scanning precession electron diffraction (SPED) [24, 25]. The results show that β″ precipitates were sheared by multiple gliding dislocations in single matrix Burgers vector steps. The shear planes were proposed to be the same as the matrix glide planes $\{111\}_{Al}$, and the precipitates were not found to be rotated even after being fragmented into discrete parts. What will happen to needle-like β″ precipitates during continuous plastic deformation until fracture (probably stronger than 20% compression), and whether they can be sheared into very small parts and rotated or not, should be studied in detail. Similar knowledge for needle-like β′ precipitates is also important but missing. The information is of significance in advancing our understanding about the plastic deformation mechanisms of many types of precipitation strengthened materials, which determines the ultimate tensile strength.

In present work, *ex-situ* and *in-situ* TEM technical are applied to study the interaction between dislocations and both β″ and β′ precipitates. *In-situ* tensile experiments in TEM allow direct observations of the dynamical microstructural evolution during deformation, and are thus used in our work. Modern *in-situ* TEM holders developed in recent years use microelectromechanical system (MEMS) devices that allow researchers to perform tensile experiments on microscale single crystal samples along controlled orientations and with controlled load or displacement, which is, a.o., very helpful for understanding samples with nanoscale precipitates. However,

in most *in-situ* TEM holders, the sample can only be tilted along one axis (parallel to the tensile direction) and observations of precipitates along another crystallographic direction (usually required) is not easy, thus supplementary *ex-situ* observations are still of key importance.

The purposes of this work are twofold: (1) to investigate the shearing behaviors and possible rotation behaviors of coherent β″ and semi-coherent β′ precipitates during the plastic stage of tensile deformation, (2) to understand the rotation mechanisms of β″ and β′ precipitates (if happened). In this work, we combine the advantages of both *in-situ* and *ex-situ* observations in TEM to investigate the evolution of β″ and β′ precipitates during the tensile deformation process of an Al-Mg-Si alloy. Atom probe tomography (APT) analysis was used to reveal the morphologies and spatial distribution of both β″ and β′ precipitates in deformed samples.

2. Methods

An Al–0.66%Mg–0.41%Si (wt.%) alloy with 0.11% Fe impurities, in the form of 1 mm thick sheets, was used for experimental investigations here. The sheets were solution heat treated at 550°C for 30 min, water quenched and aged at 180°C for 2 h, 3 h or 6 h, followed by air cooling.

Ex-situ tensile experiments were performed on an Instron 3369 testing machine (with extensometer) at room temperature and at a constant crosshead speed of 5 mm/min. The tensile samples with a gauge length of 25.0 mm and a width of 6.0 mm were cut from the 1.0 mm thick rolled sheets, and their long axes were parallel to the rolling direction.

For *ex-situ* observations of macroscopic tensile samples, TEM thin foils were prepared by electropolishing using a Tenupol 5 machine (Struers) with 30% nitric acid and 70% methanol solution at -30 ~ -35°C. It should be noted that the preparation of *ex-situ* TEM samples near the fracture region was achieved by placing a fractured sample between two Φ3 mm platinum plates, each with a Φ1 mm hole in the center (a schematic diagram is shown in Fig. S1 in the Supplementary Document). The centers of the Φ1 mm holes were located 0.5 - 1.5 mm away from the fracture tips of tensile-deformed samples. As the polished hole on the sample closest to the fracture tip is as large as Φ0.6 mm, the observed thin area is very close to the edge of the Φ1 mm area, i.e., about 0.2 - 1.2 mm away from the tip.

For *in-situ* tensile experiments, two samples of the alloy aged for 3 h were prepared by the method first developed by Samee et al. [26]. In the first step, a suitable grain with a preferred orientation $[5\bar{1}2]_{Al}$ was selected in a TEM from the thin areas of several electropolished samples. Then two parallel dog-bone samples along $[021]_{Al}$ direction were cut by FIB in a FEI Helios Nanolab 650i instrument and mounted on two push to pull (PTP) devices compatible for a Bruker Inc. PI-95 TEM picoIndenter (*in-situ* mechanical test holder). One is for measuring the stress-strain curve and the other for high-magnification observations. During the cutting and mounting procedures, the central area of every tensile sample was protected from illuminating with the ion beam, such as to minimize the effects of beam damage.

In-situ tensile experiments were performed on a FEI Osiris microscope in bright-field TEM mode operating at 200 kV with a beam current of about 2 nA. A 100 μm

conductive diamond flat puncher indenter of the single-tilt PI 95 TEM PicoIndenter was used. Tensile experiments were performed in the load control mode with a loading rate of 0.2 μN/sec. The net applied force on the specimen was determined by subtracting the contribution of the spring stiffness from the raw force. The thickness of the first sample was measured as 119.9 ± 3.6 nm by convergent beam electron diffraction (CBED) [27] before *in-situ* tension. This dogbone sample was observed in low magnification to ensure that the two ends are kept in the field of view. The second sample was not used for mechanical property measurements (thus sample thickness was not measured) and the tensile experiment was carried out at higher magnifications so that the interaction between precipitates and dislocations could be observed *in-situ*.

Ex-situ TEM observations such as selected area electron diffraction (SAED), bright field (BF) and dark field (DF) imaging as well as high-resolution TEM (HRTEM) were performed using a FEI Tecnai G2 F20 S-Twin transmission electron microscope operating at 200 kV. High angle angular dark field-scanning transmission electron microscopy (HAADF-STEM) and elemental mapping using energy-dispersive X-rays (EDX) spectroscopy were performed on a FEI Titan 80–300 Themis microscope operating at 300 kV, which is equipped with both probe and image aberration correctors and a Super-X windowless EDX detector.

APT was used to analyze the precipitates in the area about 2.3 mm away from the fracture tip of the tensile-tested sample which was aged for 6 h. The APT sample was prepared by two-step standard electropolishing procedures [28]. The first step was carried out in an electrolyte of 30 vol.% perchloric acid in acetic acid at 22 V and the

second step was carried out in an electrolyte of 5% perchloric acid in 2-butoxyethanol at 20 V. APT was performed on a LEAP-4000XSi instrument at 40 K (-233ºC) with a pulse repetition rate of 200 kHz and a detection rate of 0.5%. The pulse energy was 80 pJ. APT data were reconstructed using IVAS 3.6.8 software with a voltage range of 1500-4800 V. The precipitates were determined with iso-surfaces at 3.0 at.% Si.

3. Results

3.1 Quantitative characterizations of the precipitates

The undeformed microstructure of the Al-Mg-Si alloy aged for 3 h, is shown in Fig. 1. BF images clearly show uniformly distributed β″ precipitates elongated along $<100>_{Al}$ directions (see Fig. 1a). The average length (l) of 500 precipitates was measured as 26.4 ± 1.2 nm (average value ± standard deviation, as used throughout the whole paper). The SAED pattern shows, in addition to bright diffraction spots from the matrix crystal, the presence of extra spots with relatively weak intensity (Fig. 1b). These spots originate from β″ precipitates according to the diffraction pattern simulation by Li et al. [29], i.e. the precipitates in this alloy are mainly β″.

Figure 1c shows a HRTEM image of a β″ precipitate, which was identified from the corresponding Fast Fourier transform (FFT) pattern (Fig. 1c inset). The average cross-section area (A_{CS}) of the precipitates was measured in 60 HRTEM images and the obtained value of A_{CS} is 28.7 ± 1.7 nm^2. By taking the real needle-like morphology of β″, $r_{needle\text{-}3h}$ was calculated by the equation $A_{CS} = \pi \cdot r_{needle\text{-}3h}^2$ as 3.0 ± 0.09 nm. In the same way (details can be seen in Fig. S2 in the Supplementary Document), we obtained the value of the average radius of precipitates in the alloy aged for 2 h ($r_{needle\text{-}2h}$) as 2.18

± 0.11 nm, and the needle-like precipitates in this sample were also found to be mainly β″. The number densities of precipitates were calculated by a method based on high precision measurement of the thin foil thickness by CBED [27]. The number density of β″ and β′ precipitates in the sample aged for 6 h were reported, in our previous work [30], to be $(1.51 \pm 0.17) \times 10^{22}$ m^{-3} and $(1.12 \pm 0.12) \times 10^{22}$ m^{-3}, respectively. The ratio between these two types of precipitates was evaluated from HRTEM studies of 187 precipitates in an area. The values of the average radius of β″ precipitates ($r_{\text{needle-6h-}\beta''}$) and needle-like β′ precipitates ($r_{\text{needle-6h-}\beta'}$) were calculated as 2.43 ± 0.08 nm and 2.57 ± 0.08 nm, respectively. The precipitate sizes in these 3 samples are listed in Table 1.

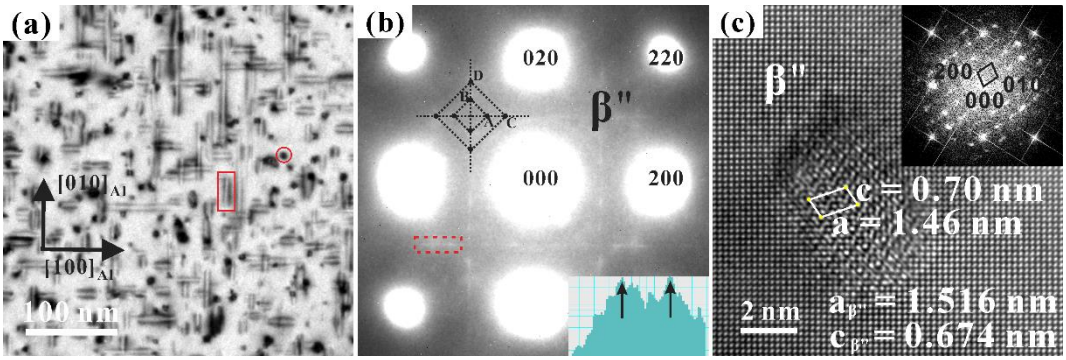

Fig. 1. TEM analysis of the undeformed microstructure of an Al-Mg-Si sample aged for 3 h at 180 ºC. (a) BF TEM image, (b) SAED pattern with the intensity profile from the red dotted box inserted, and (c) HRTEM image with corresponding FFT (inset). The electron beam is parallel to $[001]_{Al}$.

Table 1 Summary of the parameters related to quantitative characterization of the precipitates in the undeformed Al-Mg-Si samples aged at 180ºC for 2 h, 3 h and 6 h, respectively. n – number density, V_f - volume fraction.

Parameters	2 h	3 h	6 h ($N_{\beta''}$: $N_{\beta'}$ = 103 : 76)		
			β″	β′	β″ + β′
l (nm)	14.2 ± 0.6	26.4 ± 1.2	26.2 ± 1.3	22.2 ± 3.5	24.5 ± 1.3
A_{CS} (nm^2)	14.9 ± 0.2	28.7 ± 1.7	18.5 ± 1.1	20.7 ± 1.2	19.4 ± 1.2
r (nm)	2.18 ± 0.11	3.02 ± 0.09	2.43 ± 0.07	2.57 ± 0.08	2.49 ± 0.08
n (10^{22} m^{-3})	3.60 ± 0.36	1.21 ± 0.13	1.51 ± 0.17	1.12 ± 0.12	2.63 ± 0.29
V_f (%)	0.76 ± 0.11	0.92 ± 0.10	0.68 ± 0.08	0.57 ± 0.06	1.25 ± 0.14

3.2 *In-situ* observations of β″ precipitates sheared by gliding dislocations

The sample used for the *in-situ* tensile experiment was first cut from an electropolished thin foil (from the bulk sample aged for 3 h) in a zone axis close to $[5\bar{1}2]_{Al}$ with deviations less than 3° in both α and β tilt angles (of the holder), and its long axis was approximately along $[021]_{Al}$ with deviations around ± 2°. This deliberate selection produces a Schmidt factor (*m*) of 0.49, very close to the upper limit of 0.5 which corresponds to the most smooth dislocation gliding. The details of the *in-situ* tensile specimen preparation can be seen in Figs. 2a-2e, and Fig. 2f shows the geometrical schematic of the specimen.

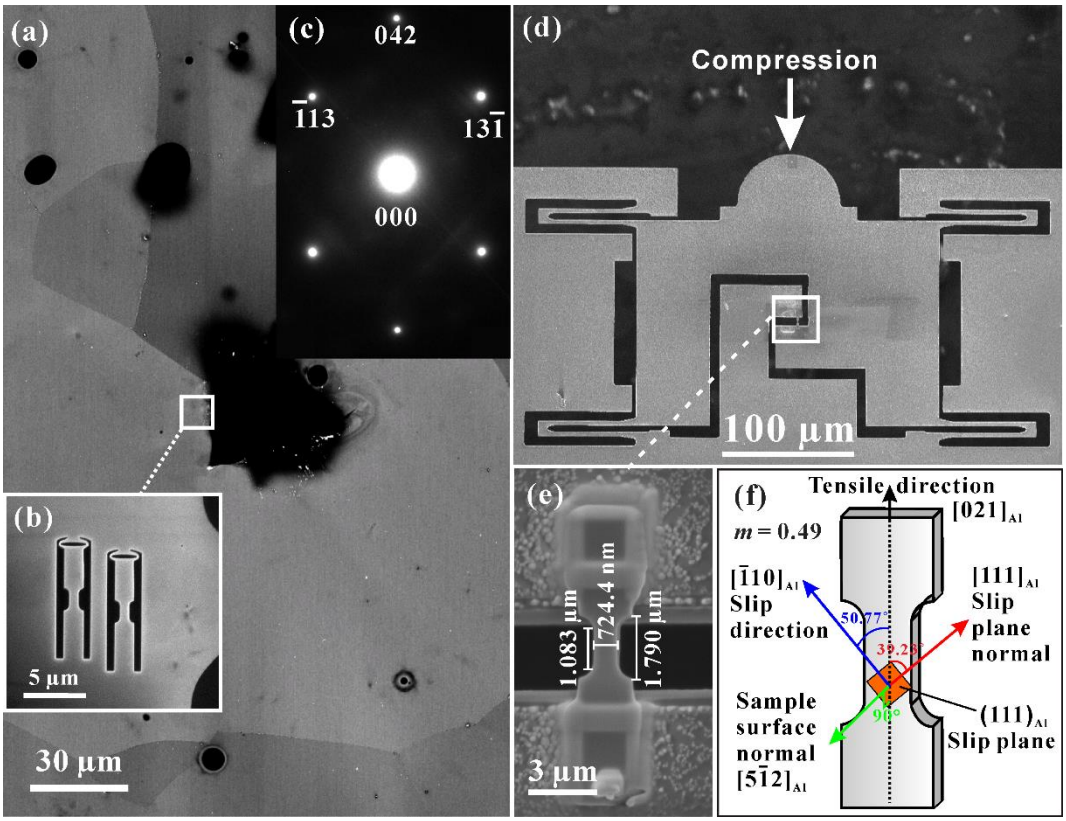

Fig. 2. Sample details for TEM *in-situ* tensile tests. (a) Back scattered electron (BSE) image of thin target area of a Φ3 mm electropolished sample. (b) Enlarged image and (c) SAED pattern of the grain from which samples for *in-situ* experiments were cut. (d) BSE image of the PTP chip used for *in-situ* TEM tensile experiments. (e) Magnified BSE image of the mounted *in-situ* sample and (f) its schematic diagram showing crystallographic directions.

A true stress-strain curve was obtained as shown in Fig. 3a, according to the method

described in Ref.[31]. The curve reveals much higher tensile strength and yield strength compared to the macro tensile curves shown in Fig. S3. This may be caused by the reduction in the number of active slip systems and dislocation density in the small size sample prepared for the *in-situ* TEM tensile experiment [32-35]. Needle-like precipitates can be observed in the BF images of Fig. 3b (before the start of the *in-situ* tensile test) and Fig. 3c (during the *in-situ* tensile test). Following the continuous stretching, the *in-situ* specimen fractured in the middle. In order to enable detailed observations of the fracture tips, the stress was kept large enough to avoid collision between the two fractured pieces upon relaxation of the PTP instrument. As shown in Fig. 3d, a new surface was formed along the edge of the fracture tip. Two types of particles were found: one is the brighter Pt particles deposited on the original sample surface when welding the two ends of the elongated thin foil sample on the PTP chip, and the other type are fine particles which might be shredded β″ precipitates inside the very thin tip. The Pt particles can be further identified by EDX and SAED as shown in Fig. S4, while the fine particles need to be further analyzed through *ex-situ* experiments due to the single α tilt condition of an *in-situ* tensile test (SAED along the $[001]_{Al}$ zone axis is not possible here) and the valley geometry of the Si PTP chip (EDX detection efficiency is low and high resolution elemental mapping is not possible). In addition, it should be noticed that no needle-like β″ precipitate was found in the fracture tip.

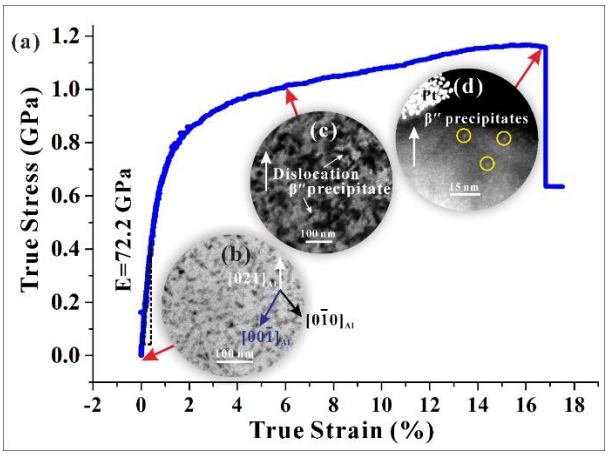

Fig. 3. Nanomechanical and microstructural evolution during the *in-situ* tensile experiment of the sample aged for 3 h. (a) True stress-strain curve, (b-c) BF images before and during the *in-situ* testing, respectively, and (d) HAADF-STEM image of the sample fracture tip after *in-situ* testing. The tensile direction $[021]_{Al}$ is shown by large white arrows.

Details of the interactions between precipitates and dislocations are shown in Fig. 4. A video showing the whole tension process is uploaded as Supplementary Video 1. The images in Fig. 4 were extracted from the video and processed via ImageJ software [36] (by *removing bright outliers* with radius = 2 pixels, threshold = 10, and *Gaussian blurring* with sigma/radius = 1.5 pixels, and then applying *auto contrast*). Five dislocations (*i*, *ii*, *iii*, *iv* and *v*) and several precipitates are marked by dotted lines and white circles, respectively. As shown in Fig. 4a, dislocations *i*, *ii*, *iii* and *iv* were temporarily impeded by precipitates *1*, *2*, *3* and *4*, respectively. Then, with the increase in tensile stress, these precipitates were sheared by the further gliding of these previously impeded dislocations, as shown in Fig. 4b. In this step, dislocations *i*, *ii* and *iii* were impeded by precipitates *2*, *3* and *4*, respectively. Immediately after this step, precipitate *2* was sheared by dislocation *i* (see Fig. 4c), and as a result of further tension, precipitates *3* and *4* were sheared by dislocations *ii* and *iii* (see Fig. 4d), respectively.

In the stage corresponding to Fig. 4d, dislocations *i* and *ii* were hindered by precipitates *3* and *4*, respectively. Figs. 4e-4h are the unmarked images of Figs. 4a-4d, respectively, added for clarity. Obviously, each of the 3 precipitates (*2*, *3*, and *4*) was sheared twice by visible dislocations during the 3.2 s of continuous tension.

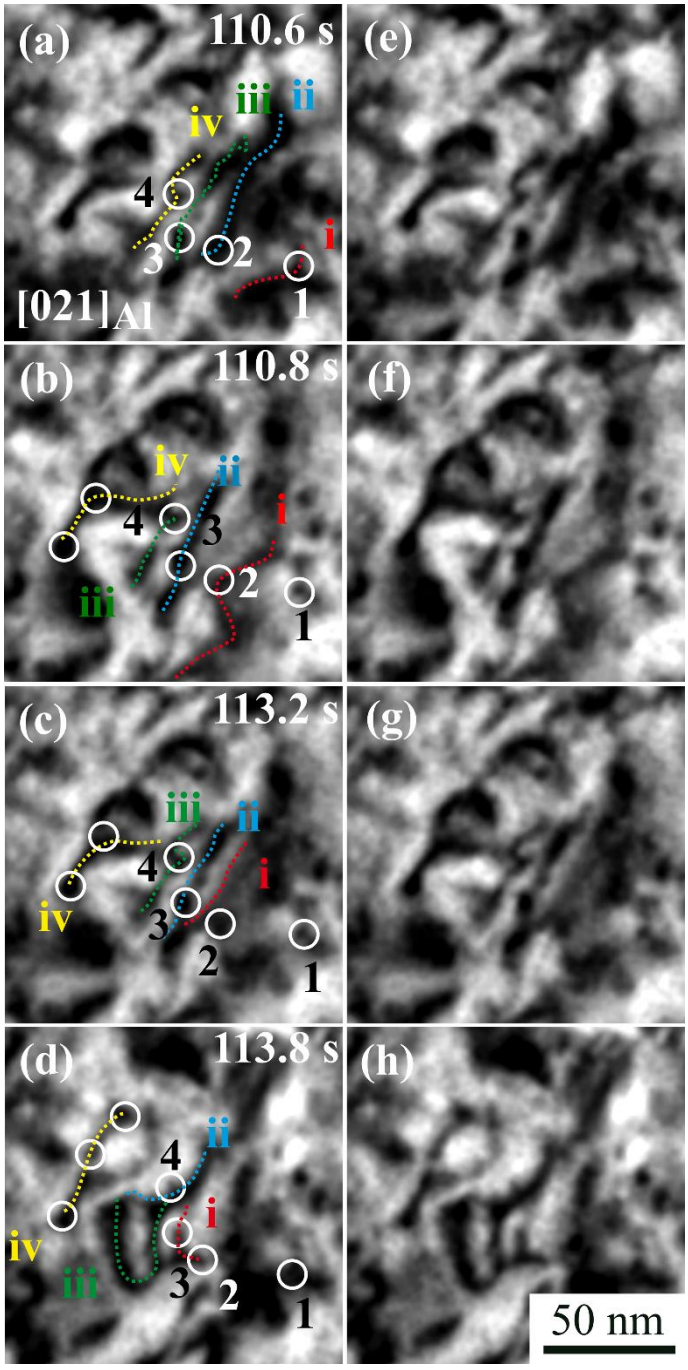

Fig. 4. *In-situ* BF observation of the interaction between dislocations (colored lines, Roman numbers) and β″ precipitates (white circles, Arabic numbers) during tension of the microscale sample (aged for 3 h) at a constant high magnification. (a)-(d) Video

frames captured during the *in-situ* tensile deformation under a constant load rate of 0.2 μN/s until the sample breaks. The unmarked images of (a)-(d) are shown in (e)-(h), respectively.

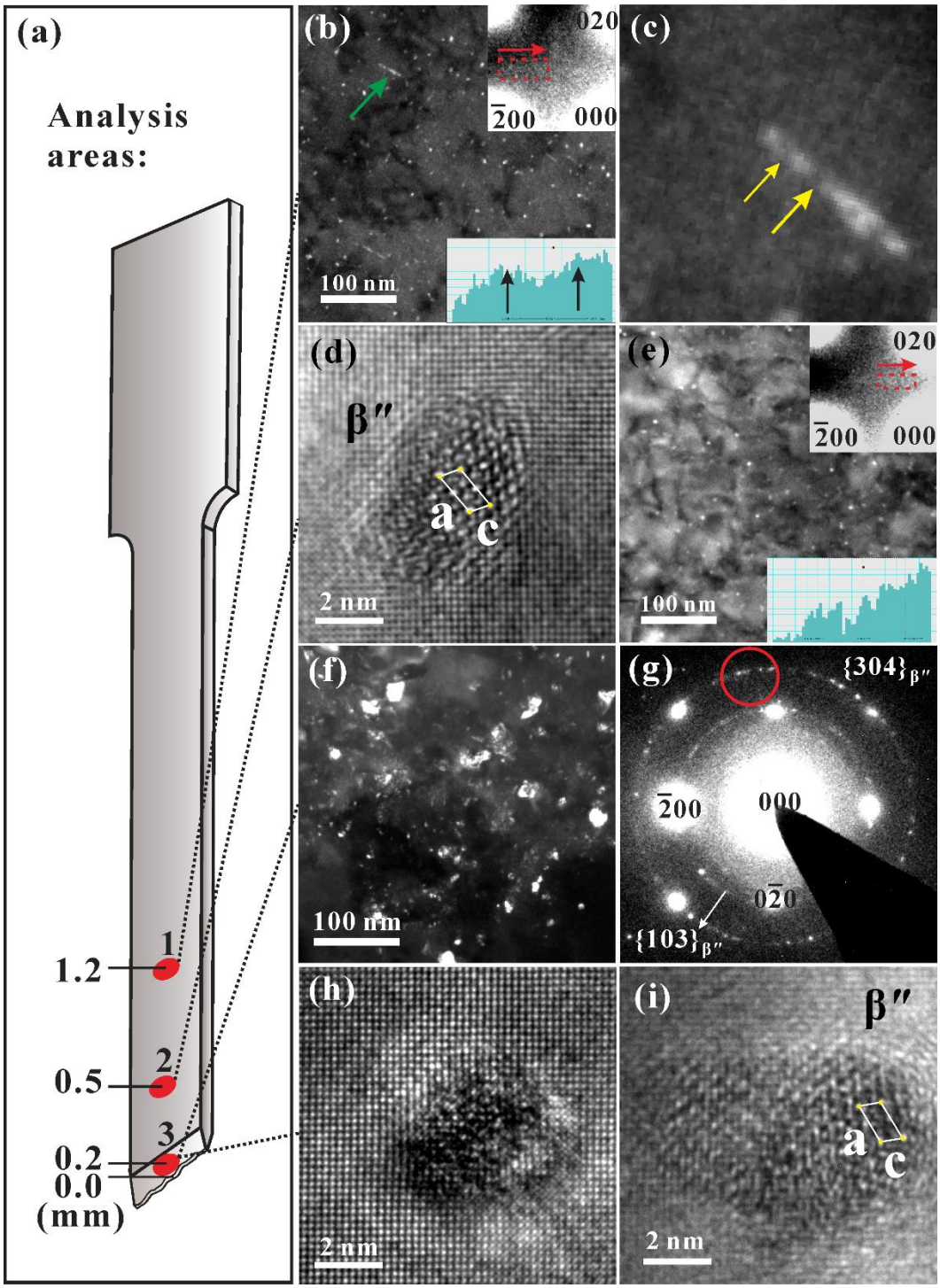

Fig. 5. *Ex-situ* TEM observation of the areas in (a) a fractured sample after ageing for 3 h and macro tensile test, which are about 1.2 mm (b-d), 0.5 mm (e) and 0.2 mm (f-i) away from the fracture tip. (b) and (e) dark field images using the diffraction spots denoted by arrows in the corresponding SAED patterns inserted. The intensity profiles from the red dotted boxes are also inserted. In addition, the green arrow in (b) marks a sheared needle-like β″ precipitate which is shown at a higher magnification in (c). (d)

HRTEM image of a β″ precipitate in (b). (f) Dark field image of the fracture tip (only 0.2 mm away), and (g) the corresponding SAED pattern. (h) and (i) HRTEM images of two precipitates in the facture tip. In (h) the observation direction was $[001]_{Al}$ while in (i) it was $[010]_{\beta''}$, which was achieved after further tilting the sample by about 3° from $[001]_{Al}$.

3.3 *Ex-situ* TEM evidence for fragmentation and rotation of β″ precipitates during deformation

An *ex-situ* TEM sample cut from a fractured specimen after a macro tensile test was electropolished and the area observed in TEM was about 1.2 mm away from the fracture tip (area 1 in Fig. 5a). Needle-like β″ precipitates can be found in the dark field images as shown in Fig. 5b. The precipitate denoted by the green arrow is enlarged in Fig. 5c, showing the trace left by shearing (marked by yellow arrows). The β″ precipitate can still be characterized from the HRTEM image in Fig. 5d and the coherent growth direction along $[010]_{\beta''}//[001]_{Al}$ is well maintained. In contrast, in the TEM sample taken from the position about 0.5 mm away from the fracture tip (area 2 in Fig. 5a), no needle-like precipitate can be found in the dark field image in Fig. 5e, precipitates were all fragmented due to shearing by dislocations. The cross-shaped diffraction signals from precipitates can still be found in the zoom of the SAED pattern inserted in Fig. 5b, the signal got much weaker for the area shown in Fig. 5e. This is confirmed by the red dotted box scans in Fig. 5b and Fig. 5e where the two peaks are more apparent for Fig. 5b compared to Fig. 5e. These two peaks are the same to those in the red dotted box in Fig. 1b (the undeformed sample), which are more apparent though. This indicates that part of the precipitates in these two samples with some distance from the fracture tip are still maintaining their orientation relationships (ORs)

with the Al matrix.

In the area very close to the fracture tip (area 3 in Fig. 5a), as shown in Fig. 5f, the precipitates are also fragmented. Besides, there are no visible cross-shaped diffraction spots from precipitates in the SAED pattern in Fig. 5g. It is worth mentioning that polycrystalline diffraction rings of β″, indexed as $\{103\}_{\beta''}$ and $\{304\}_{\beta''}$, have appeared in the pattern. These rings unambiguously reveal that the β″ precipitates were sheared into small parts and they lost their initial OR with the Al matrix, i.e., they have been rotated. Meanwhile, most precipitates cannot be characterized by HRTEM as typically shown in Fig. 5h, which was obtained exactly along $[001]_{Al}$. In addition, once the zone axis of observation deviates by ~3° from $[001]_{Al}$, some pieces of β″ precipitates can be characterized from the HRTEM image as typically shown in Fig. 5i, where the Al lattice fringes are only visible along one direction. The deviation is also seen from the FFT of the Al matrix near the precipitate as shown in Fig. S5.

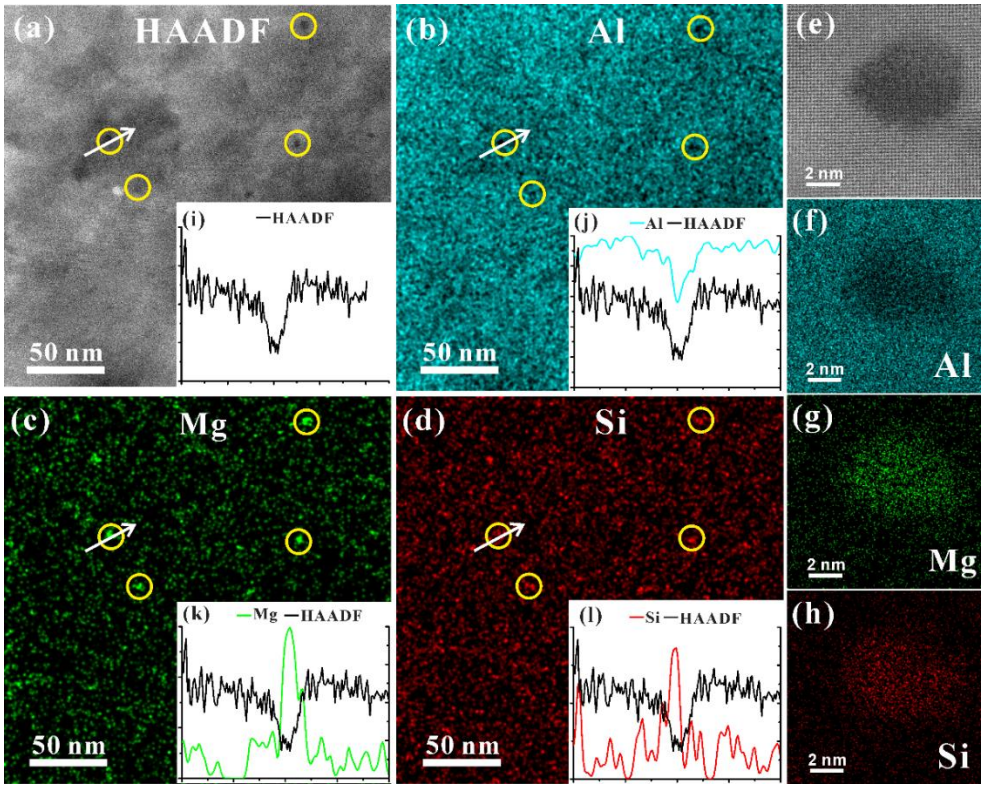

Fig. 6. *Ex-situ* TEM analysis of the fracture tip, corresponding to area 3 in Fig. 5. (a)-(d) and (e)-(h) STEM-EDX results at low and high magnifications, respectively. (i)-(l) Line profiles across a β″ precipitate (indicated by a white arrow, more details are shown in Fig. S6).

The EDX elemental maps of Figs. 6a and 6e are (also from area 3 in Fig. 5a) shown in Figs. 6b-6d and Figs. 6f-6h, respectively. It is seen that the fine particles in Figs. 6a and 6e are rich in Mg and Si. Therefore, these particles are identified as shredded β″ precipitates and they no longer have the needle-like shape.

3.4 Complementary *Ex-situ* TEM and APT studies of sheared β″ and β′ precipitates

The TEM results of the area very close to the fracture tip of the sample aged for 2 h were similar to those of the sample aged for 3 h in that only equiaxed shapes (see Fig. 7a) and polycrystalline diffraction rings (see Fig. 7b) of β″ precipitates can be found. Therefore these needle-like precipitates were also sheared into small parts and rotated. It should be noted that the $\{304\}_{\beta''}$ diffraction rings in Fig. 7b and also in Fig. 5g do not

coincide with the $\{220\}_{Al}$ spots, and there is a small shift between them as denoted by the black cross (indicating the center of the reflection)and the dashed arc in Fig. 7b. On the contrary, some precipitates (β″ and/or β′) in the area very close to the fracture tip of the sample aged for 6 h were sheared into small parts but their needle-like shape can still be recognized, while some other precipitates were intact, as shown in Fig. 7c. It should be noted that both β″ [29] and β′ [37], in their characteristic orientations, produce crossed shaped diffraction spots among Al spots. As the needle-like morphologies of precipitates can be identified in the dark field image in Fig. 7c using the diffraction signals in the red circle in Fig. 7d, it is inferred there were indeed β″/β′ diffraction signals but they were too weak to be recorded by the Gatan Model 832 CCD camera used. Therefore, it is reasonable to speculate that some precipitates still maintain their original characteristic orientation relationship with the matrix in this tensile-deformed sample.

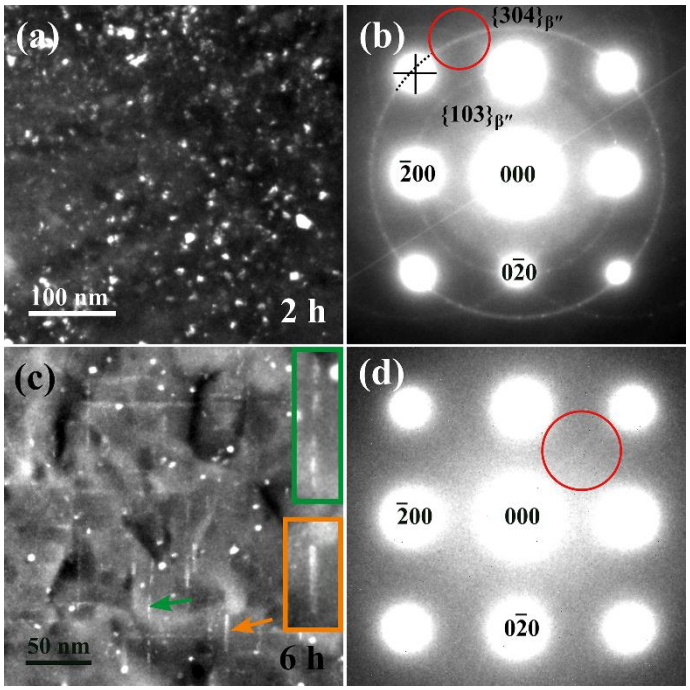

Fig. 7. *Ex-situ* TEM observations of the areas about 0.2 mm away from the fracture tips

of the tensile-tested samples which were aged for 2 h (a-b) and 6 h (c-d). (a) and (c) Dark-field images, (b) and (d) corresponding SAED patterns. The diffraction signals in red circles were used for dark field imaging.

The frequencies of r_{needle} (equivalent radius of the cross-section) of the needle-like precipitates, in the undeformed samples aged for 2 h, 3 h and 6 h, are shown in Fig. 8. The values of $r_{needle\text{-}2h}$, $r_{needle\text{-}3h}$, $r_{needle\text{-}6h\text{-}\beta''}$ and $r_{needle\text{-}6h\text{-}\beta'}$ were measured from 84, 60, 104 and 77 HRTEM images of the precipitates, respectively. It is clear that the distribution of $r_{needle\text{-}6h\text{-}\beta''}$ is completely between the distributions of $r_{needle\text{-}2h}$ and $r_{needle\text{-}3h}$ (for β″). The distribution of $r_{needle\text{-}6h\text{-}\beta'}$ resembles that of $r_{needle\text{-}6h\text{-}\beta''}$ except 3.9% of β′ precipitates exceed the radius range of β″ precipitates. Since the β″ precipitates were fragmented and rotated in the areas very close to the fracture tip of the samples aged for 2 h and 3 h, this should hold true for β″ precipitates with very similar sizes in the similarly treated sample aged for 6 h. Therefore, it is inferred that the precipitates retaining a needle-like shape in the deformed sample aged for 6 h are β′.

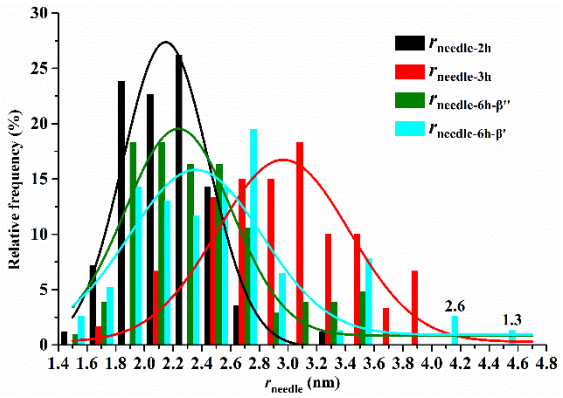

Fig. 8. The distribution of r_{needle} of the precipitates in the undeformed samples aged for different times. The histogram shows the frequency counts of $r_{needle\text{-}2h}$ (in black), $r_{needle\text{-}3h}$ (in red), $r_{needle\text{-}6h\text{-}\beta''}$ (in green) and $r_{needle\text{-}6h\text{-}\beta'}$ (in blue) with corresponding Gaussian fitting curves.

APT characterization of a tip specimen made close to the fracture surface of a tensile-tested sample aged for 6 h are shown in Fig. 9. The analyzed volume contains

precipitates with various sizes and morphologies including needles, short needles and equiaxed particles. It is known that the typical β″-$Mg_5Al_2Si_4$ precipitate has a Mg/Si ratio of 1.25 [38], smaller than 1.8 of the β′-Mg_9Si_5 precipitate [39]. Our TEM characterization of the sample under the same aging condition (but undeformed) confirmed that the $V_{f\text{-}6h\text{-}\beta''}/V_{f\text{-}6h\text{-}\beta'}$ ratio is 0.68/0.57 [30]. In order to differentiate precipitates observed in the APT analyzed volume, particles with Mg/Si ratios smaller than 1.9 were considered to be β″, the others with higher Mg/Si ratios are considered to be β′. Interestingly, the volume fraction ratio of the two groups of precipitates was found to be 0.64/0.57, close to 0.68/0.57 measured by TEM. Both the average Mg/Si ratios (the dashed lines in Figs. 9b and 9c) of the two groups of precipitates detected by APT are a little higher than the standard Mg/Si ratios of β″ and β′ precipitates by 0.25~0.35. This is largely due to some small fragments of β′ detected with low Mg/Si ratios failed to be picked out correctly by our method. Wrong classification of them into β″ group would push the average Mg/Si ratio higher as a result. Such difficulty in APT measurement is mainly due to that the detection efficiency is only about 55% for LEAP 4000X SI and large scattering in Mg/Si ratios of small features detected is expected. It is important to notice that most of (20/23, i.e. 87%) of the particles smaller than 200 nm^3 are β″ precipitates, and 8 of them with individual volumes less than 30 nm^3. Combined with our previous work that the smallest volume of precipitates is 68.1 nm^3 in the undeformed sample under the same aging condition [30], one can deduce that the particles with sizes less than 30 nm^3 which are inside the analyzed volume (not cut by the surface of the analyzed volume) are broken pieces of β″ precipitates (see the light

green ellipse mark in Fig. 9c). In another word, the current APT results confirm that β″ precipitates are much easier than β′ precipitates to be sheared into small pieces by gliding dislocations during tensile deformation.

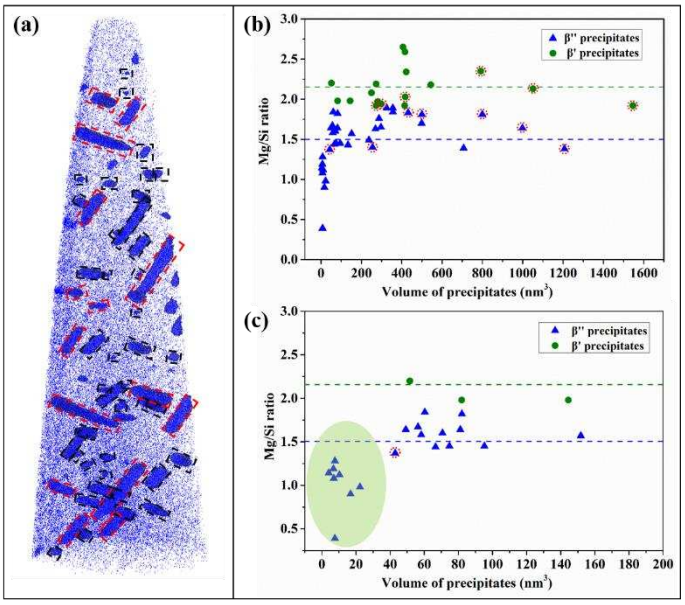

Fig. 9. APT studies of precipitates in an area about 2.3 mm away from the fracture tip of the tensile-deformed sample aged for 6 h. (a) A reconstructed volume of $90 \times 90 \times 286$ nm^3 with precipitates, which are visualized by adding iso-composition surfaces of 3.0 at.% Si. (b) The Mg/Si ratio vs the volume of each β″ or β′ precipitate, over 53 precipitates in total. (c) Mg/Si ratio vs volume of each small β″ and β′ precipitate (over 23 precipitates) with its volume less than 200 nm^3. The precipitates marked with black dotted rectangles are in the APT needle tip sample, those marked with red dotted rectangles are not completely embedded in the current tip. The data points marked with red dotted circles in (b-c) correspond to the precipitates marked with red dotted rectangles in (a).

4. Discussion

4.1 The shearable nature of the β″ precipitate in its size range

The face-centered cubic (fcc) Al matrix has 12 slip systems consisting of {111} slip planes and <110> slip directions [40]. When the resolved shear stress of a slip system is greater than its critically resolved shear stress, dislocations will start to slip on the slip systems during deformation [41]. These moving dislocations will shear the β″

precipitates in Al-Mg-Si alloys, and cross slip will occur among screw dislocations [14]. With increasing the level of deformation, the segments of precipitates were continuously being sheared. In this work it has been verified that β″ precipitates are shearable, and the critical precipitate radius for the transition from shearable to non-shearable interactions is found larger than 6.75 nm or 4.0 nm in the sphere model or the needle model, respectively. Our results thus strongly imply that β″ should be considered as shearable when modelling mechanical properties, since the β″ precipitates observed here are the largest that one can find in the literature [8, 13, 14, 20]. Our findings support previous investigations in which β″ precipitates were found to grow and coarsen but remain shearable when aging proceeds [13, 14]. The details of the shearing mechanism of β″ precipitates can be found in Ref. [25].

4.2 Mechanisms lying behind different shearing and rotation behaviors between β″ and β′ precipitates

It is reported that dislocations shearing weakens coherent precipitates but strengthens semi-coherent precipitates [9]. The resistance of a coherent precipitate to secondary shear is reduced after the principle shear of the precipitate [42, 43]. Thus, dislocations can shear multiple times at the same location in a coherent precipitate, but this is quite difficult for semi-coherent precipitates because the new interfaces caused by dislocation shearing are with large misfit. As a result, a higher slip localization can be achieved in alloys strengthened by coherent precipitates than in alloys strengthened by semi-coherent precipitates [9, 44]. The coherent β″ precipitates are thus fragmented as displayed in Figs. 10a-10b, and the corresponding mechanism is schematically

shown in Figs. 10d-10g.

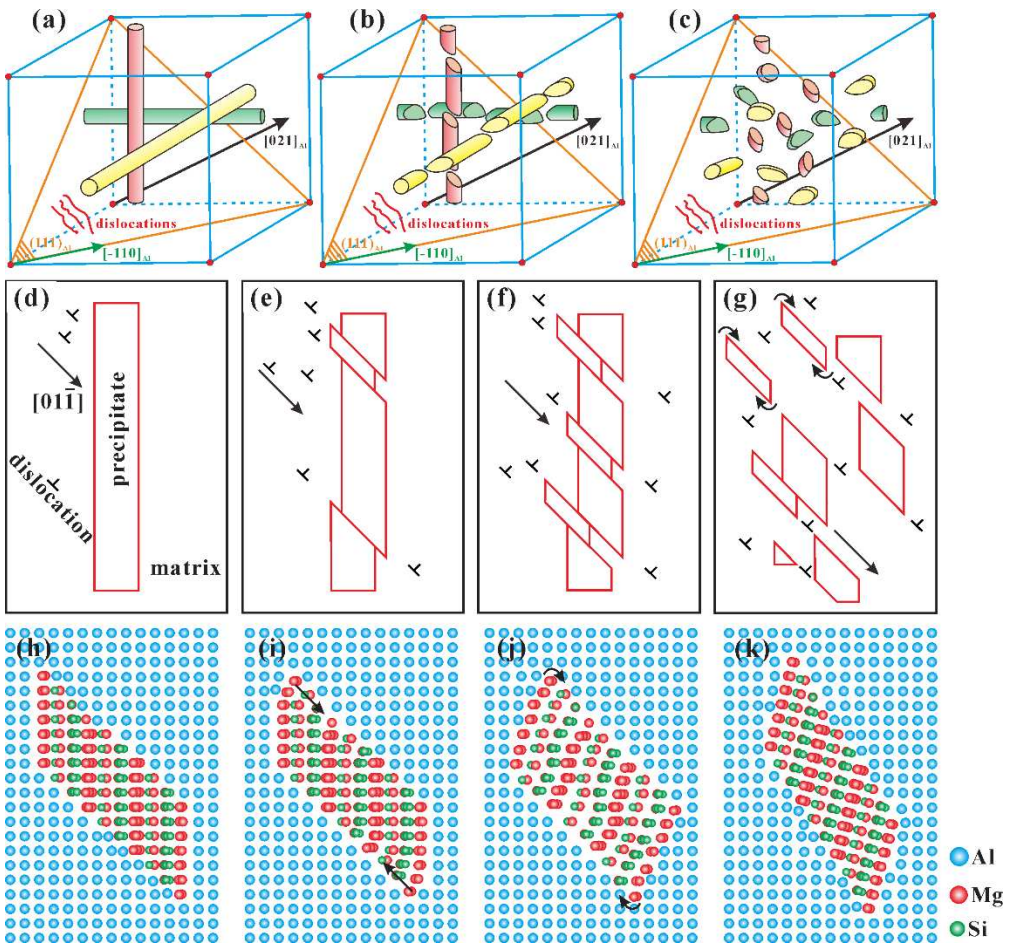

Fig. 10. Schematic diagram of the consequences of the interaction between precipitates and dislocations. (a) Precipitates before the interaction with dislocations. (b) Precipitates are sheared by dislocations. (c) Precipitates are further shredded into small parts which lose the initial ORs with the Al matrix. The mechanism of precipitates being sheared by dislocations is shown in (d) - (h). Black arrows represent gliding of dislocations along $[01\bar{1}]_{Al}$. (i) - (l) The proposed mechanism for rotation of (small parts of) precipitates by GB sliding mediated by diffusion. Large angles are used here to visualize the rotations.

In contrast, in the case of our work, slip localization of semi-coherent β′ precipitates was found to be difficult, and most of them cannot be fragmented under the similar deformation which breaks apart coherent β″ precipitates. A more severely mismatched

interface and a step with stronger strain field around it will be created after the less coherent β′ is being sheared by dislocations. The highly strained interface then becomes a high energy boundary, which is not energetically favorable [9]. As a result, the rotation mechanism through slip localization, as proposed by Guétaz and Pénisson [23], can hardly be activated for β′ precipitates in this work. This can explain why β′ precipitates can basically maintain the original OR with the Al matrix and mostly keep in needle-like shape, while β″ precipitates were fragmented and rotated during similar tensile deformation processes.

4.3 The rotation mechanism of fragmented β″ precipitates

The recent SPED work of Christiansen et al. [24, 25] on sheared β″ precipitates in an 20% compressed Al-Mg-Si alloy revealed that the precipitates are fragmented into small parts while the original needle-like shape can still be recognized, this is a state very close to that shown in Figs. 5b-5c. They proved the non-existence of rotation of these parts compared to the original OR at this stage, as diffraction spots of these parts are still within the cross-shaped diffraction characteristics of unsheared β″ precipitates. It is thus inferred that the rotation of discrete β″ precipitate parts observed in this work occurred in a deformation condition more severe than in their work. In other words, further shearing are required to rotate the just-fragmented β″ precipitates. Thus, the rotation mechanism during fragmentation of semi-coherent precipitates through multiple shears, as discovered by Guétaz and Pénisson [23], cannot explain the rotation of coherent β″ precipitates observed in this work.

At the atomic scale, there are mainly 3 mechanisms leading to grain rotation, i.e.

(1) climb of grain boundary (GB) dislocations towards triple-joint (TJ) points [45] and free surfaces, (2) cross-grain glide of dislocations [46], and (3) GB sliding through diffusional processes [47-49]. The first mechanism is not possible in our *ex-situ* experiments because in a large Al grain (~ 80 μm) with nano-precipitates embedded inside, the TJ points and the free surfaces of the millimeter-scale sample are too far away from a dislocation at a precipitate/matrix boundary. The second mechanism through cross-grain glide of dislocations has already been denied by the findings of Christiansen et al. [24, 25], it indeed occurred (from the matrix to the precipitate and then to the matrix) and caused the fragmentation of β″ precipitates, but there was no rotation, probably due to the coherent nature of the interface structures. GB sliding can occur because diffusion is very active during deformation of aluminum even at room temperature. For instance, in the work of Hutchinson et al. [50], vacancies were injected into cyclically deformed solution-heat-treated Al alloys at room temperature, and precipitates were formed without a real aging process. Besides, the heterophase boundaries existing in this work are more preferable for sliding than homophase boundaries [51]. Furthermore, a more recent work reported rise of temperature to 1250-2450°C in the shear band during quasi-static loading of a titanium alloy at room temperature [52]. Traces of shear bands were also found in the current alloy (see Figs. S7 and S8 in the Supplementary Document), deformed either *in-situ* or *ex-situ*. In the current aluminum alloy with a relatively low melting point around 650°C, a slight rise in temperature can notably increase the probability of diffusion and GB sliding, resulting in the rotation of precipitate parts. The rotation process of the coherent β″

precipitate parts is shown in the schematics of Figs. 10b-10c and explained in Figs. 10h-10k. In the current stage, the precipitate parts are speculated to rotate a very small angle each time and rotation accumulates step by step to a large angle. Our discovery of the rotation of coherent fine nano-precipitates in a plastic Al matrix during deformation expands our knowledge on the alloy's deformation. However, future *in-situ* analysis of the rotation mechanism at the atomic scale remains worthwhile.

5. Conclusions

The interaction between β″ precipitates and dislocations during tensile deformation of an Al-Mg-Si alloy was systematically investigated by the *in-situ* and *ex-situ* TEM observations as well as APT studies, and placed in comparison to that of β′ precipitates. These two types of precipitates showed different shearing and rotation behaviors, and the interaction mechanisms were discussed. Detailed findings are as follows:

(1) β″ nano-precipitates can be sheared into fragments by gliding dislocations during deformation. The β″ precipitates, which are observed in this work, with needle radius as large as 4 nm, were all found sheared and no intact precipitate could be found. As these are almost the largest β″ precipitates found in the literature, it is inferred that all β″ precipitates are shearable. In the just-fragmented state, the β″ fragments maintain their original OR with the matrix.

(2) With continuous increase of deformation and the corresponding increase in number of shearing dislocations, coherent β″ precipitates were further sheared into fine discrete equiaxed particles and rotated, until the sample fractured. As

a result, their initial OR with the matrix changed. This is probably mediated via the precipitate/matrix boundary sliding facilitated by diffusion, a different mechanism from that proposed previously for semi-coherent precipitates through slip localization.

(3) The semi-coherent β′ precipitates can also be sheared by dislocations but the probability was much lower than that of β″. They can basically maintain the needle-like shape and their original OR with the matrix. This is mainly due to the fact that the interfaces with higher energies, which is formed after the less coherent β′ precipitates being sheared by dislocations, is not energetically favorable compared to those of β″ precipitates. Slip localization is more difficult for β′ precipitates and thus almost no subsequent rotation can happen.

Supplementary Data

Supplementary data are available online.

Acknowledgement

This work was financially supported by the National Natural Science Foundation of China (52071340, 51711530713 and 51820105001), the Flemish Science Foundation (FWO; VS.026.18N) and the Fundamental Research Funds for the Central Universities (WUT: 2019III012GX, 2020III002GX). The authors thank the EMAT lab at UA, the Center for Materials Research and Analysis and the State Key Laboratory of Silicate

Materials for Architectures at WUT, as well as the Advanced Research Center at CSU for use of TEMs.

Author contributions

M.J.Y. and A.O. contributed equally to this work. K.L., Y.D. and D.S. designed the project and guided the research. M.J.Y. conducted the *ex-situ* TEM experiments. A.O. and V.S. conducted the *in-situ* TEM experiments with M.J.Y. and K.L.. Z.Y.H. conducted STEM-EDX experiments. M. F. and S.B.J conducted APT experiment. M.J.Y. and A.O. wrote the initial draft. K.L., M.S., G.S., Y.D., G.V.T. and D.S. finalised the paper. All authors contributed to extensive discussions of the results.

Competing interests

The authors declare no competing interests.

References

[1] C. Puncreobutr, A. B. Phillion, J. L. Fife, P. Rockett, A. P. Horsfield, P. D. Lee. In situ quantification of the nucleation and growth of Fe-rich intermetallics during Al alloy solidification, Acta Mater. 79 (2014) 292-303.

[2] Edwards GA, Stiller K, Dunlop GL, C. MJ. The precipitation Sequence in Al-MgSi Alloys, Acta Mater. 46 (1998) 3893-3904.

[3] C. D. Marioara, H. Nordmark, S. J. Andersen, R. Holmestad. Post-β" phases and their influence on microstructure and hardness in 6xxx Al-Mg-Si alloys, J. Mater. Sci. 41 (2006) 471-478.

[4] H. W. Zandbergen, S. J. Andersen, J. Jansen. Structure determination of Mg5Si6 particles in Al by dynamic electron diffraction studies, Science. 277 (1997) 1221.

[5] L. Ding, Z. Jia, J. F. Nie, Y. Weng, L. Cao, H. Chen, X. Wu, Q. Liu. The structural and compositional evolution of precipitates in Al-Mg-Si-Cu alloy, Acta Mater. 145 (2018) 437-450.

[6] S. Wenner, R. Holmestad. Accurately measured precipitate–matrix misfit in an Al–Mg–Si alloy by electron microscopy, Scr. Mater. 118 (2016) 5-8.

[7] K. Teichmann, C. D. Marioara, S. J. Andersen, K. Marthinsen. TEM study of β′ precipitate interaction

mechanisms with dislocations and β’ interfaces with the aluminium matrix in Al–Mg–Si alloys, Mater. Charact. 75 (2013) 1-7.
[8] M. Vivas, P. Lours, C. Levaillant, A. Couret, M. J. Casanove, A. Coujou. Determination of precipitate strength in aluminium alloy 6056-T6 from transmission electron microscopyin situstraining data, Philos. Mag. A. 76 (1997) 921-931.
[9] B. Q. Li, F. E. Wawner. Dislocation interaction with semicoherent precipitates (Ω phase) in deformed Al–Cu–Mg–Ag alloy, Acta Mater. 46 (1998) 5483-5490.
[10] F. Delmas, J. Majimel, M. Vivas, G. Molenat, A. Couret, A. Coujou. Cross-slip and glide in {001} planes of Al-Mg-Si alloy 6056, Philos. Mag. Lett. 83 (2003) 289-296.
[11] F. Delmas, M. Vivas, P. Lours, M. J. Casanove, A. Couret, A. Coujou. Straining mechanisms in aluminium alloy 6056. In-situ investigation by transmission electron microscopy, Mater. Sci. Eng. A. 340 (2003) 286-291.
[12] P. Donnadieu, G. F. Dirras, J. Douin. An approach of precipitate/dislocation interaction in age-hardened Al-Mg-Si Alloys: measurement of the strain field around precipitates and related simulation of the dislocation propagation, Mater. Sci. Forum. 396-402 (2002) 1019-1024.
[13] W. J. Poole, X. Wang, D. J. Lloyd, J. D. Embury. The shearable–non-shearable transition in Al–Mg–Si–Cu precipitation hardening alloys: implications on the distribution of slip, work hardening and fracture, Philos. Mag. 85 (2005) 3113-3135.
[14] K. Misumi, K. Kaneko, T. Nishiyama, T. Maeda, K. Yamada, K.-i. Ikeda, M. Kikuchi, K. Takata, M. Saga, K. Ushioda. Three-dimensional characterization of interaction between β” precipitate and dislocation in Al–Mg–Si alloy, J. Alloy. Compd. 600 (2014) 29-33.
[15] T. Saito, C. D. Marioara, S. J. Andersen, W. Lefebvre, R. Holmestad. Aberration-corrected HAADF-STEM investigations of precipitate structures in Al–Mg–Si alloys with low Cu additions, Philos. Mag. 94 (2013) 520-531.
[16] E. Hornbogen, E. A. S. Jr. Overview no. 102 Theory assisted design of high strength low alloy aluminum, Acta Metall. Mater. 41 (1993) 1-16.
[17] L. Proville, B. Bakó. Dislocation depinning from ordered nanophases in a model fcc crystal: From cutting mechanism to Orowan looping, Acta Mater. 58 (2010) 5565-5571.
[18] S. Esmaeili, D. J. Lloyd, W. J. Poole. A yield strength model for the Al-Mg-Si-Cu alloy AA6111, Acta Mater. 51 (2003) 2243-2257.
[19] O. R. Myhr, Ø. Grong, S. J. Andersen. Modelling of the age hardening behaviour of Al–Mg–Si alloys, Acta Materialia. 49 (2001) 65-75.
[20] X. Wang, J. D. Embury, W. J. Poole, S. Esmaeili, D. J. Lloyd. Precipitation strengthening of the aluminum alloy AA6111, Metall. Mater. Trans. A. 34 (2003) 2913-2924.
[21] C. Xu, M. Furukawa, Z. Horita, T. G. Langdon. Using ECAP to achieve grain refinement, precipitate fragmentation and high strain rate superplasticity in a spray-cast aluminum alloy, Acta Mater. 51 (2003) 6139-6149.
[22] M. Murayama, Z. Horita, K. Hono. Microstructure of two-phase Al–1.7 at% Cu alloy deformed by equal-channel angular pressing, Acta Mater. 49 (2001) 21-29.
[23] L. Guétaz, J. Pénisson. High resolution electron microscopy of a deformed superalloy: shear of precipitates, Mater. Sci. Eng. A. 175 (1994) 141-148.
[24] E. Christiansen, C. D. Marioara, B. Holmedal, O. S. Hopperstad, R. Holmestad. Nano-scale characterisation of sheared β" precipitates in a deformed Al-Mg-Si alloy, Scientific Reports. 9 (2019) 17446.

[25] E. Christiansen, C. D. Marioara, I. G. Ringdalen, R. Bjørge, B. Holmedal, O. S. Hopperstad, R. Holmestad, A. Deschamps, J. C. Ehrström, P. Jarry, G. Salloum-Abou-Jaoude, L. Salvo, C. Sigli. Detailed investigation of the shearing mechanism of β" precipitates in Al-Mg-Si alloys, MATEC Web of Conferences. 326 (2020) 01005.
[26] V. Samaeeaghmiyoni, H. Idrissi, J. Groten, R. Schwaiger, D. Schryvers. Quantitative in-situ TEM nanotensile testing of single crystal Ni facilitated by a new sample preparation approach, Micron. 94 (2017) 66-73.
[27] K. Li, H. Idrissi, G. Sha, M. Song, J. Lu, H. Shi, W. Wang, S. P. Ringer, Y. Du, D. Schryvers. Quantitative measurement for the microstructural parameters of nano-precipitates in Al-Mg-Si-Cu alloys, Mater. Charact. 118 (2016) 352-362.
[28] D. J. Larson, T. J. Prosa, R. M. Ulfig, B. P. Geiser, T. F. Kelly. Specimen Preparation. In: Larson DJ, Prosa TJ, Ulfig RM, Geiser BP, Kelly TF, editors. Local Electrode Atom Probe Tomography: A User's Guide. New York, NY: Springer New York, 2013. p.25-53.
[29] K. Li, M. Song, Y. Du, H. Zhang. Simulation of the electron diffraction patterns from needle/rod-like precipitates in Al–Mg–Si alloys, Mater. Charact. 62 (2011) 894-903.
[30] M. Yang, H. Chen, A. Orekhov, Q. Lu, X. Lan, K. Li, S. Zhang, M. Song, Y. Kong, D. Schryvers, Y. Du. Quantified contribution of β'' and β' precipitates to the strengthening of an aged Al–Mg–Si alloy, Mater. Sci. Eng. A. 774 (2020) 138776.
[31] H. Idrissi, A. Kobler, B. Amin-Ahmadi, M. Coulombier, M. Galceran, J.-P. Raskin, S. Godet, C. Kübel, T. Pardoen, D. Schryvers. Plasticity mechanisms in ultrafine grained freestanding aluminum thin films revealed by in-situ transmission electron microscopy nanomechanical testing, Appl. Phys. Lett. 104 (2014) 101903.
[32] C. Zhou, I. J. Beyerlein, R. LeSar. Plastic deformation mechanisms of fcc single crystals at small scales, Acta Mater. 59 (2011) 7673-7682.
[33] Y. Xiang, J. J. Vlassak. Bauschinger and size effects in thin-film plasticity, Acta Mater. 54 (2006) 5449-5460.
[34] M. Yaghoobi, G. Z. Voyiadjis. Size effects in fcc crystals during the high rate compression test, Acta Mater. 121 (2016) 190-201.
[35] W. Xu, L. P. Dávila. Size dependence of elastic mechanical properties of nanocrystalline aluminum, Mater. Sci. Eng. A. 692 (2017) 90-94.
[36] C. A. Schneider, W. S. Rasband, K. W. Eliceiri. NIH Image to ImageJ: 25 years of image analysis, Nat Methods. 9 (2012) 671-675.
[37] W. Yang, M. Wang, X. Sheng, Q. Zhang, L. Huang. Precipitate characteristics and selected area diffraction patterns of the β' and Q' precipitates in Al–Mg–Si–Cu alloys, Philos. Mag. Lett. 91 (2011) 150-160.
[38] S. Wenner, L. Jones, C. D. Marioara, R. Holmestad. Atomic-resolution chemical mapping of ordered precipitates in Al alloys using energy-dispersive X-ray spectroscopy, Micron. 96 (2017) 103-111.
[39] R. Vissers, M. A. van Huis, J. Jansen, H. W. Zandbergen, C. D. Marioara, S. J. Andersen. The crystal structure of the β' phase in Al–Mg–Si alloys, Acta Mater. 55 (2007) 3815-3823.
[40] A. G. Jackson. Slip systems. In: Jackson AG, editor. Handbook of Crystallography: For Electron Microscopists and Others. New York, NY: Springer New York, 1991. p.83-88.
[41] G. Gottstein. Physical foundations of materials science: Springer Science & Business Media, 2013.
[42] T. H. Sanders, E. A. Starke. The effect of slip distribution on the monotonic and cyclic ductility of Al-Li binary alloys, Acta Metall. 30 (1982) 927-939.

[43] E. Hornbogen, K. H. Zum Gahr. Distribution of plastic strain in alloys containing small particles, Metallography. 8 (1975) 181-202.
[44] B. Zhang, L. Wu, B. Wan, J. Zhang, Z. Li, H. Gou. Structural evolution, mechanical properties, and electronic structure of Al–Mg–Si compounds from first principles, J. Mater. Sci. 50 (2015) 6498-6509.
[45] L. Wang, J. Teng, P. Liu, A. Hirata, E. Ma, Z. Zhang, M. Chen, X. Han. Grain rotation mediated by grain boundary dislocations in nanocrystalline platinum, Nat. Commun. 5 (2014) 4402.
[46] V. Yamakov, D. Wolf, S. R. Phillpot, A. K. Mukherjee, H. Gleiter. Deformation-mechanism map for nanocrystalline metals by molecular-dynamics simulation, Nat. Mater. 3 (2004) 43-47.
[47] I. A. Ovid'ko, A. G. Sheinerman. Special rotational deformation in nanocrystalline metals and ceramics, Scr. Mater. 59 (2008) 119-122.
[48] J. W. Cahn, J. E. Taylor. A unified approach to motion of grain boundaries, relative tangential translation along grain boundaries, and grain rotation, Acta Mater. 52 (2004) 4887-4898.
[49] D. Moldovan, D. Wolf, S. R. Phillpot. Theory of diffusion-accommodated grain rotation in columnar polycrystalline microstructures, Acta Mater. 49 (2001) 3521-3532.
[50] W. Sun, Y. Zhu, R. Marceau, L. Wang, Q. Zhang, X. Gao, C. Hutchinson. Precipitation strengthening of aluminum alloys by room-temperature cyclic plasticity, Science. 363 (2019) 972.
[51] M. E. Kassner. Fundamentals of creep in metals and alloys: Butterworth-Heinemann, 2015.
[52] L. Choisez, L. Ding, M. Marteleur, H. Idrissi, T. Pardoen, P. J. Jacques. High temperature rise dominated cracking mechanisms in ultra-ductile and tough titanium alloy, Nat. Commun. 11 (2020).

Figure(s)

Click here to access/download;Figure(s);Fig. 1.tif

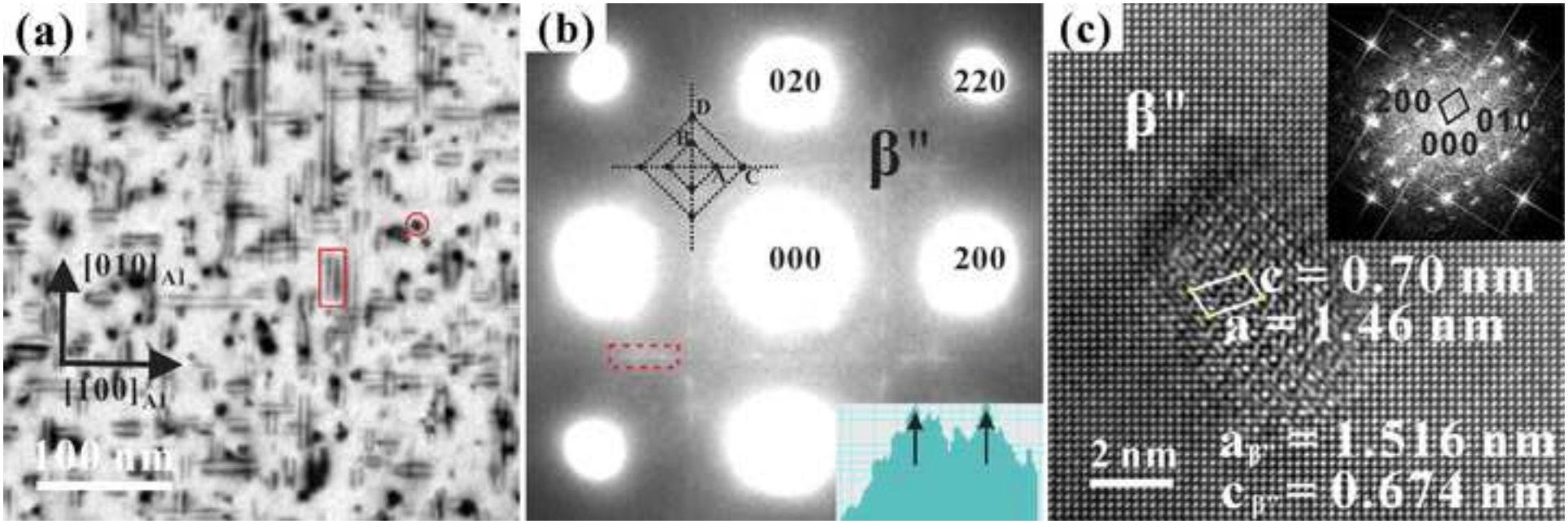

Figure(s)

Click here to access/download;Figure(s);Fig. 2.tif

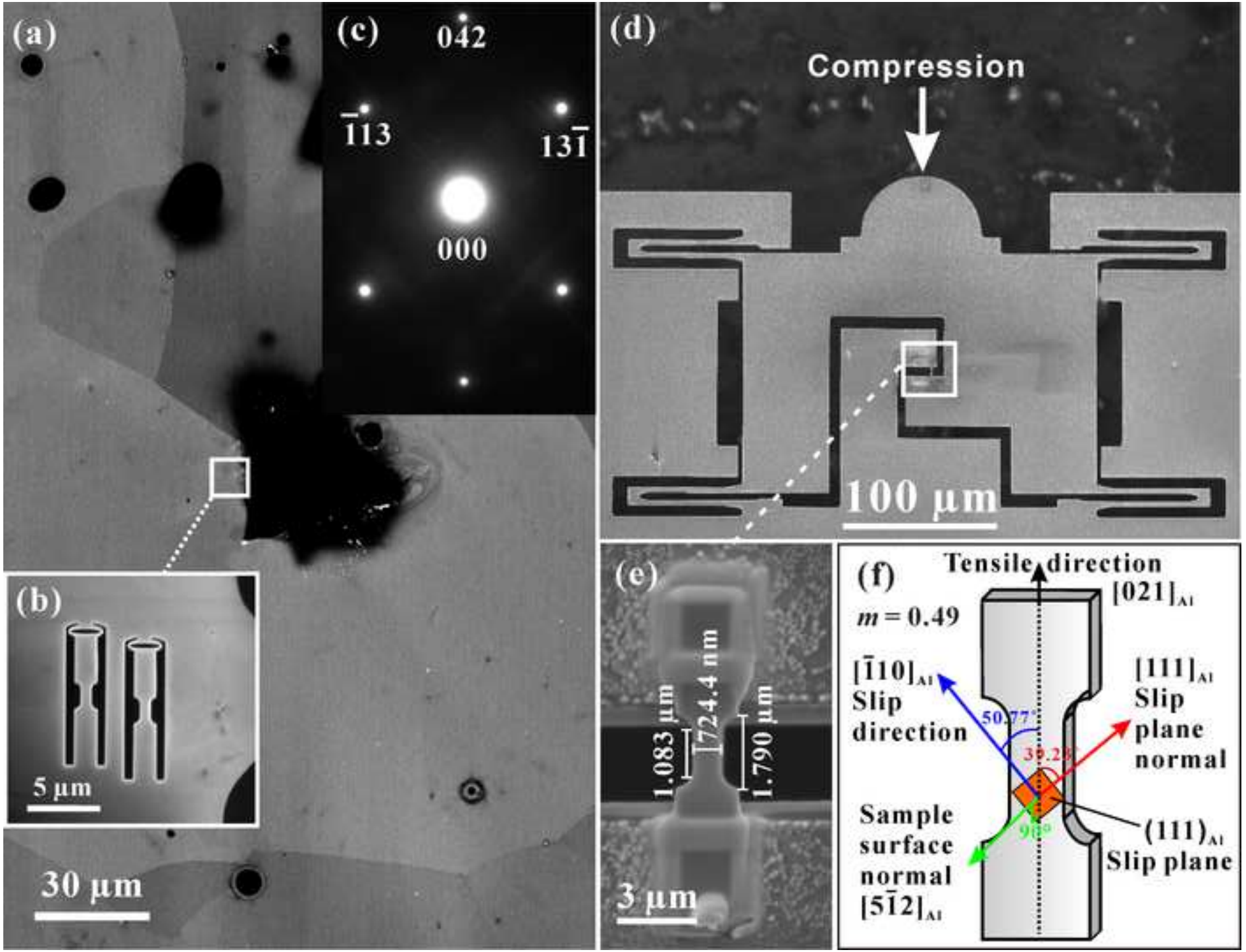

Figure(s)

Click here to access/download;Figure(s);Fig. 3.tif

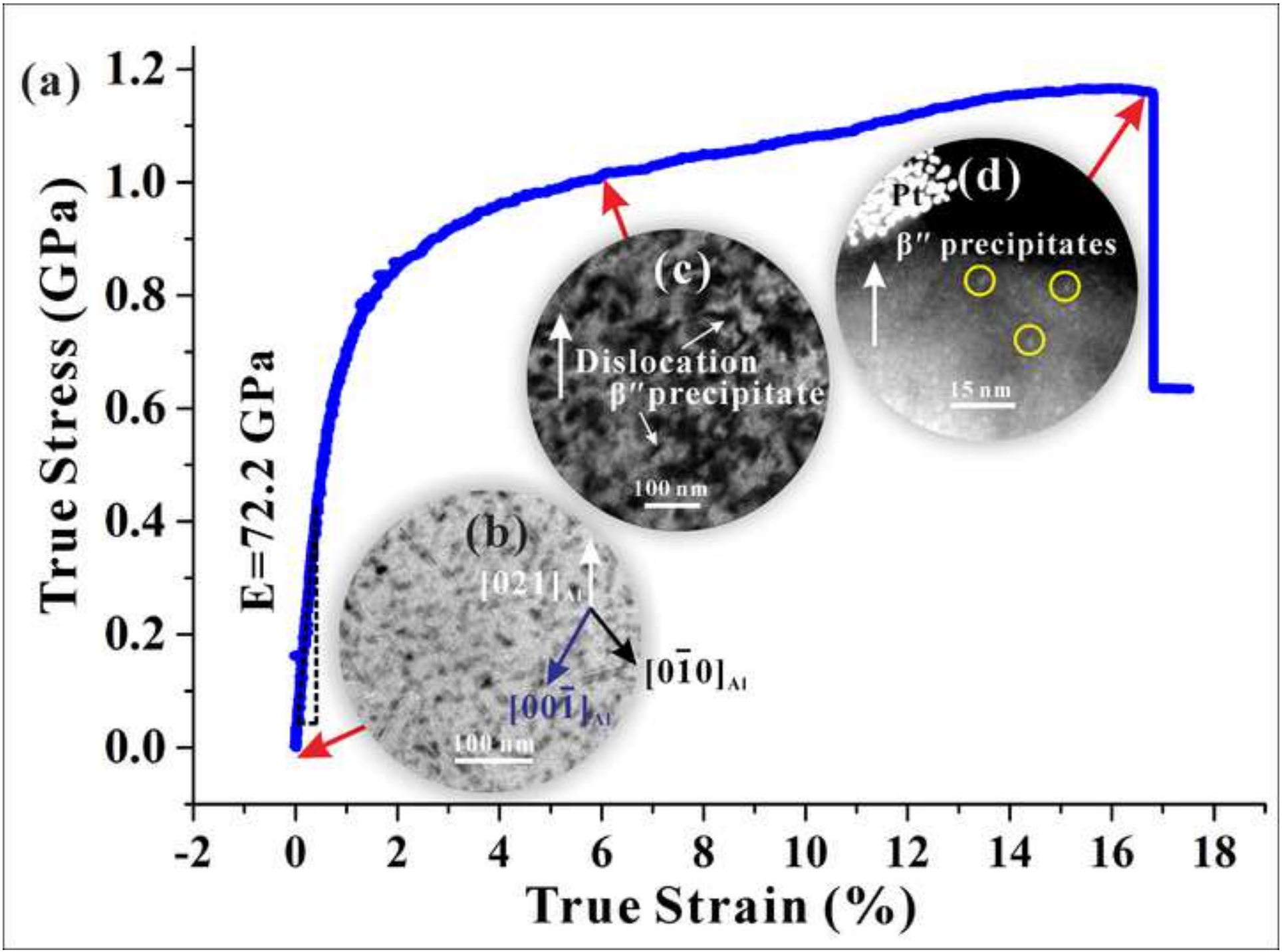

Figure(s)

Click here to access/download;Figure(s);Fig. 4.tif

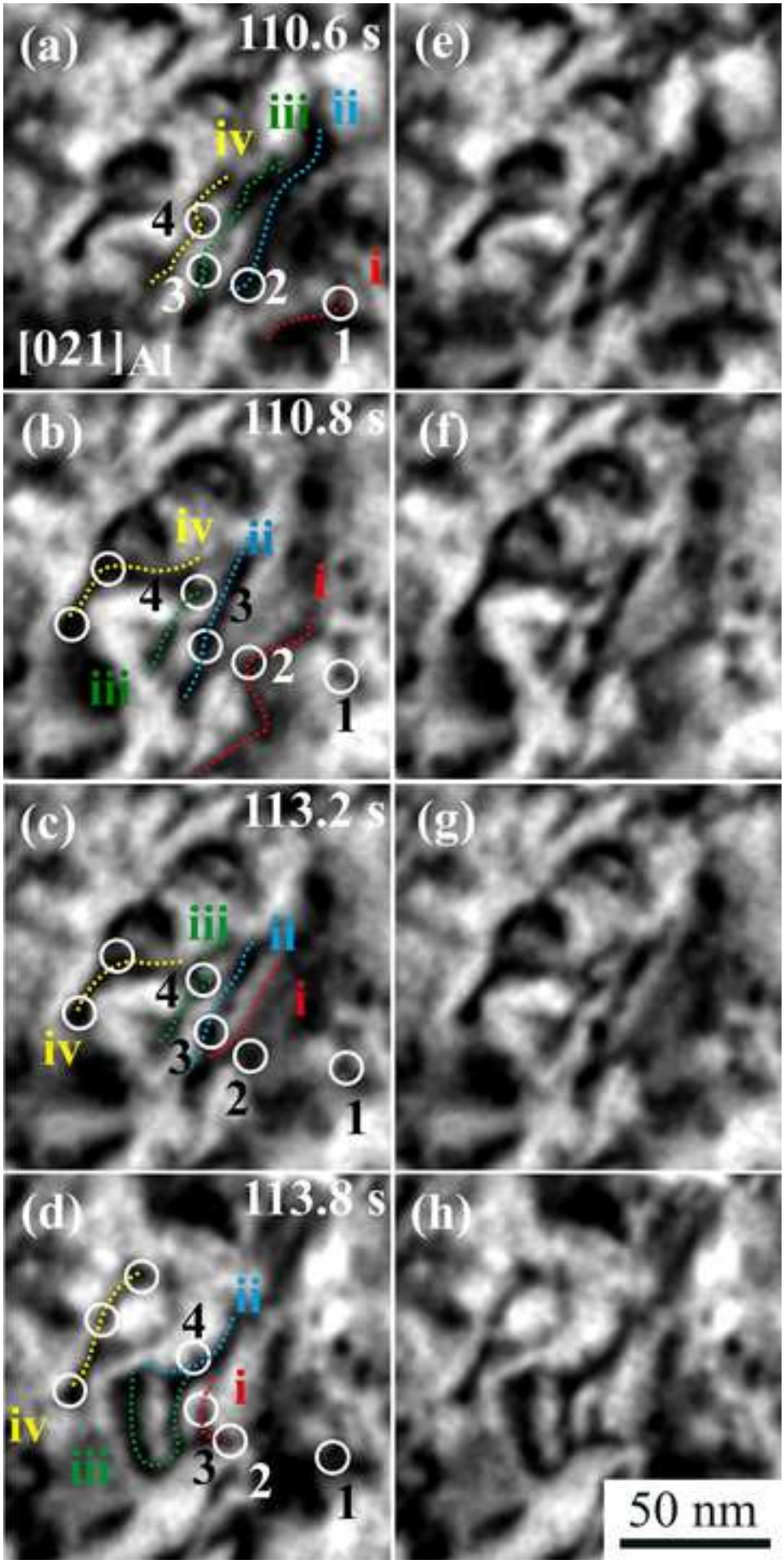

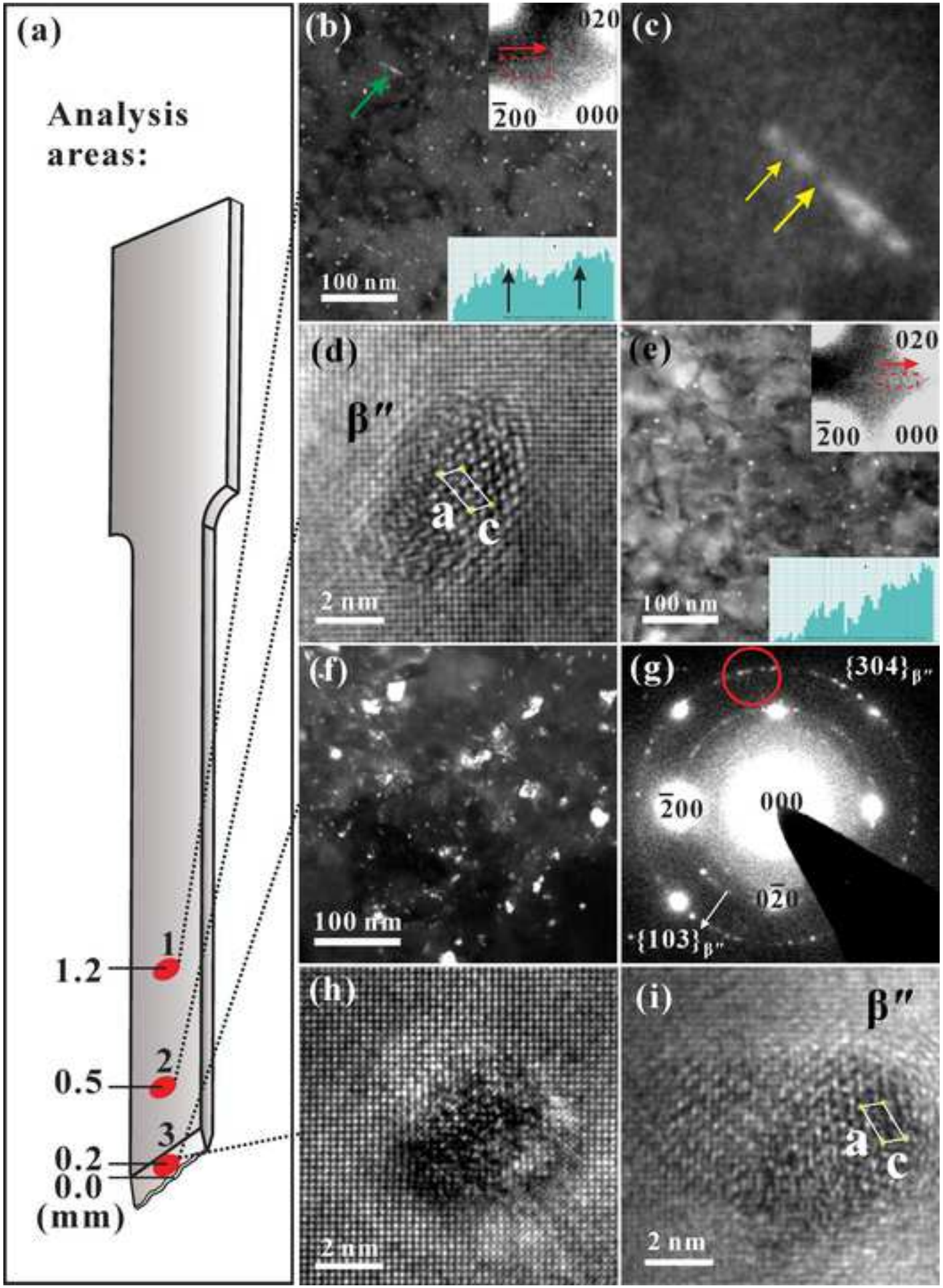
(a)
Analysis areas:
1
1.2
2
0.5
3
0.2
0.0
(mm)
(b)
020
$\bar{2}$00
000
100 nm
(c)
(d)
β″
a
c
2 nm
(e)
020
$\bar{2}$00
000
100 nm
(f)
100 nm
(g)
{304}β″
$\bar{2}$00
000
0$\bar{2}$0
{103}β″
(h)
2 nm
(i)
β″
a
c
2 nm

Figure(s)

Click here to access/download;Figure(s);Fig. 6.tif

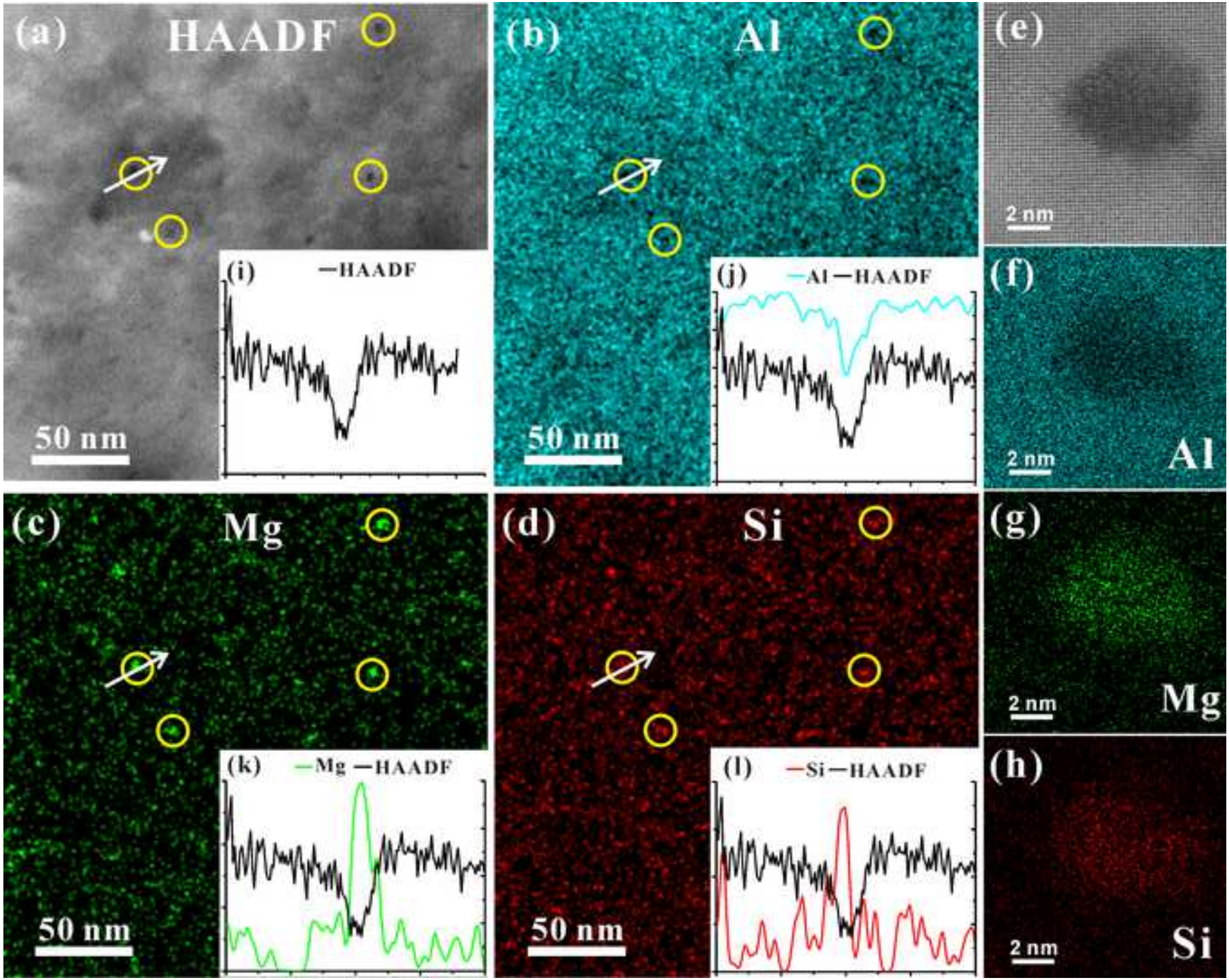

Figure(s)

Click here to access/download;Figure(s);Fig. 7.tif

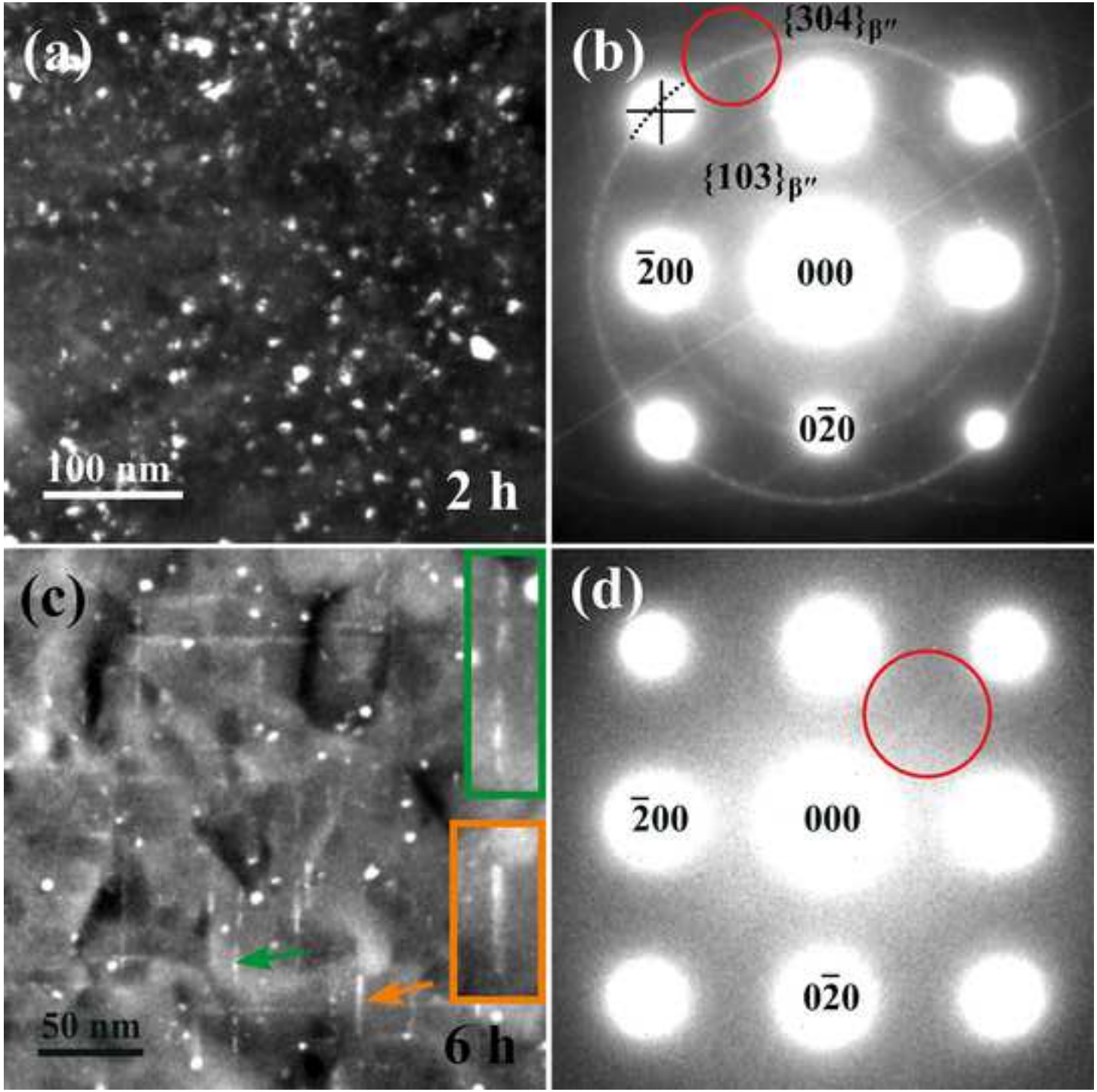

Figure(s)

Click here to access/download;Figure(s);Fig. 8.tif

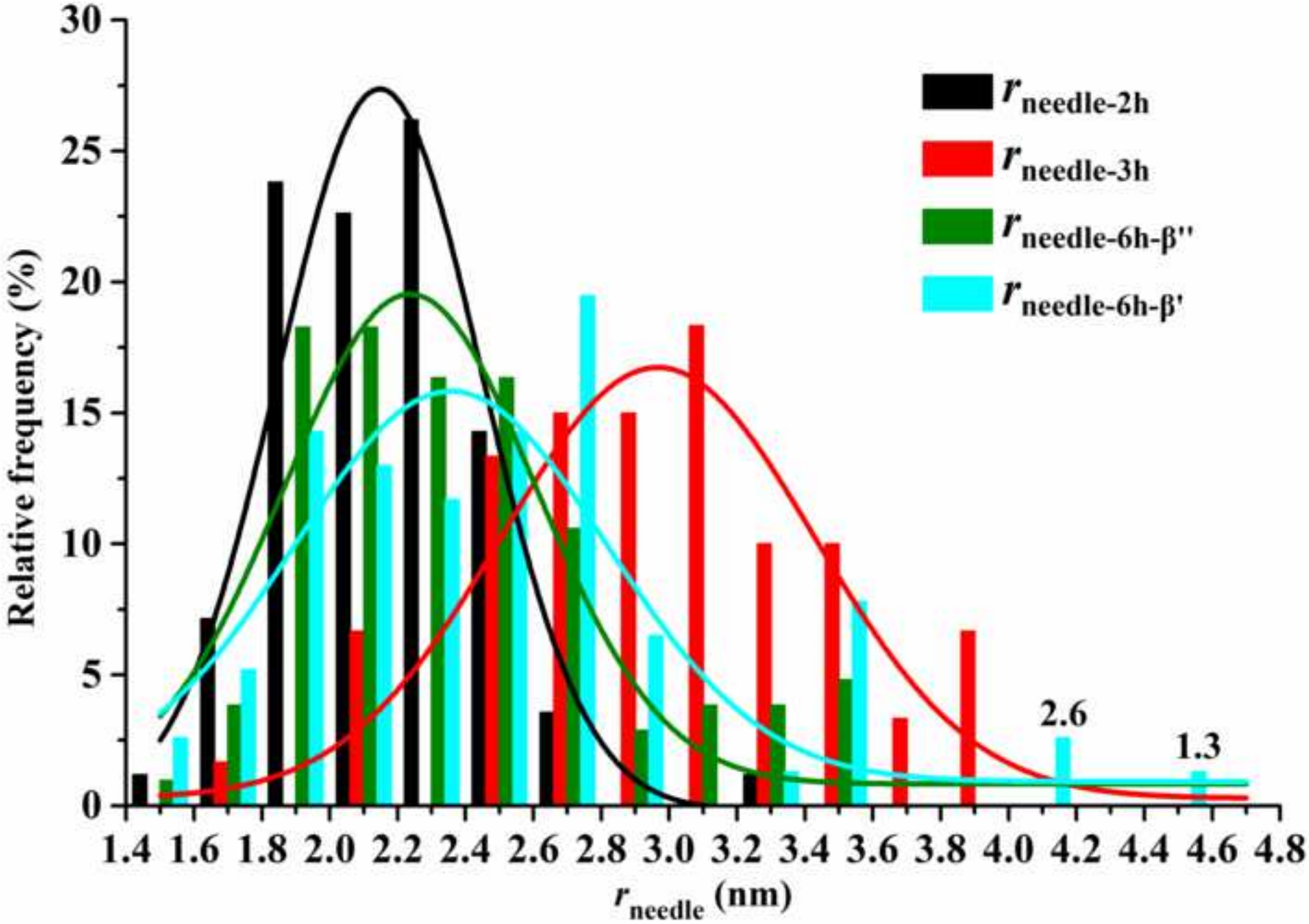

Figure(s)

Click here to access/download;Figure(s);Fig. 9.tif

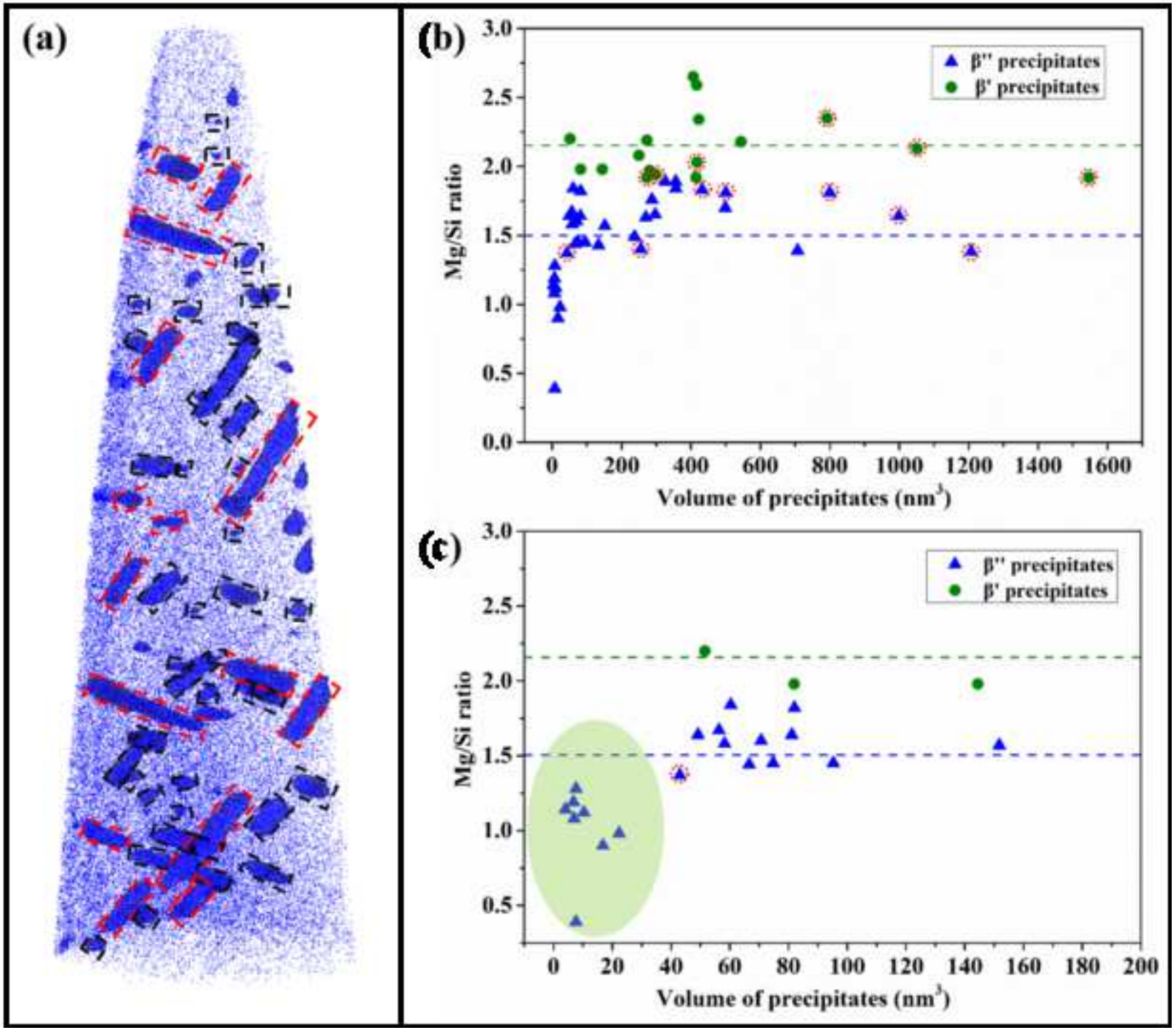

Figure(s)

Click here to access/download;Figure(s);Fig. 10.tif

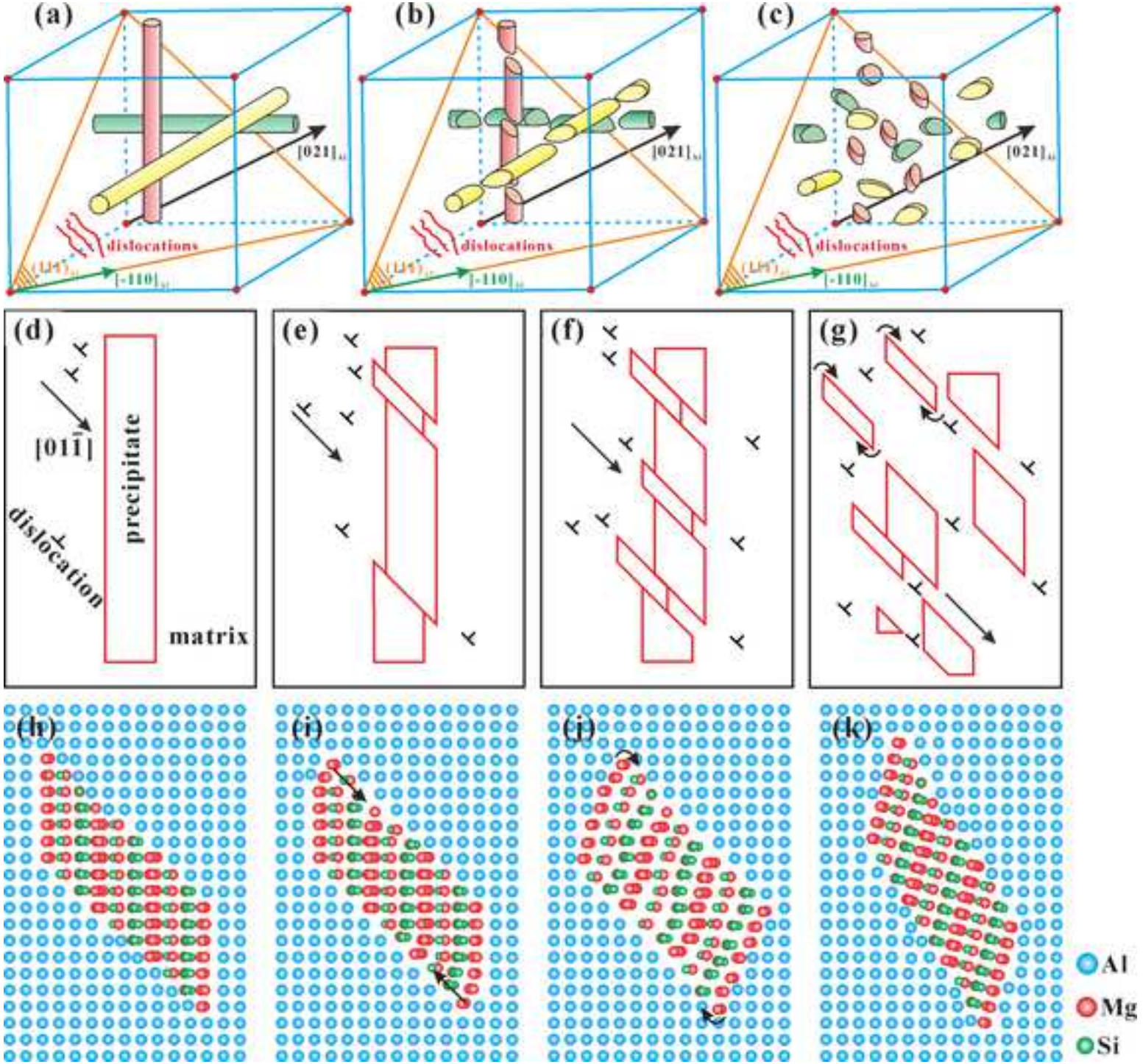

Graphical Abstract

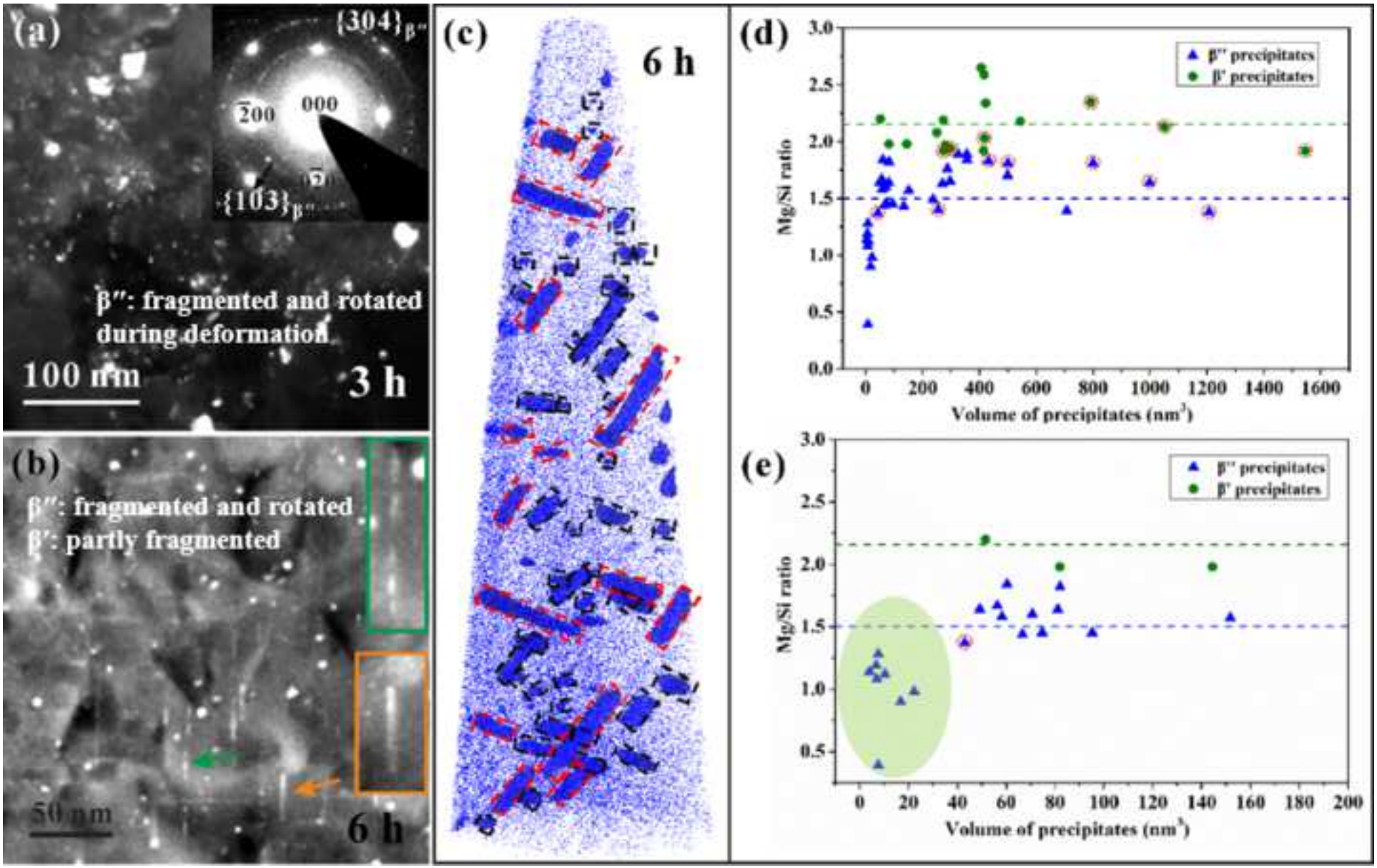

Video Still

Click here to access/download

Video Still

Supplementary video 1.mov

Click here to access/download

Video Still

Supplementary video 2.mov

Declaration of interests

☒ The authors declare that they have no known competing financial interests or personal relationships that could have appeared to influence the work reported in this paper.

☐The authors declare the following financial interests/personal relationships which may be considered as potential competing interests:
